Key Points:
- A magnetostratigraphy for the 1,600-m-thick sedimentary and volcanic sequence at International Ocean Discovery Program Site U1438 is presented
- We produced a high-resolution age model and sedimentation rates for Site U1438
- We reconstructed the ages of the emplacement, rise, and death of the Kyushu-Palau arc in the Philippine Sea Plate

Correspondence to:
M. Maffione,
m.maffione@bham.ac.uk

Timing of Tectonic and Magmatic Events in the Philippine Sea Plate Since 50 Ma From High-Resolution Magnetostratigraphy of IODP Site U1438

Marco Maffione[1] and **Antony Morris[2]**

[1]School of Geography, Earth, and Environmental Sciences, University of Birmingham, Birmingham, UK, [2]School of Geography, Earth, and Environmental Sciences, Plymouth University, Plymouth, UK

Abstract The Philippine Sea Plate in the West Pacific is a unique natural laboratory to study subduction dynamics and the evolution of upper plate magmatism following subduction initiation. To investigate these processes, International Ocean Discovery Program Expedition 351 recovered at Site U1438, located in a rear-arc position, a complete sedimentary sequence from recent age to the early Eocene and the top of the underlying volcanic basement. The recovered cores offered the opportunity to study for the first time and in unprecedented detail the styles, products, and timing of the volcanic events that marked the emplacement, growth, and demise of the Kyushu-Palau volcanic arc following the inception of the Izu-Bonin-Mariana subduction. Here, we report a magnetostratigraphy for Site U1438 based on ∼60,000 remanence directions isolated from 1,063 archive half core sections and 429 discrete specimens. We identified 142 magnetic reversals and correlated 115 of them with the geomagnetic polarity timescale. When combined with additional biostratigraphic and geochronological constraints, our magnetostratigraphy allowed construction of a high-resolution age model for Site U1438 and the determination of changes in sedimentation rates. We show that following subduction initiation at 52–50 Ma and the emplacement of basalts in the rear-arc at 48.7 Ma, a diffuse volcanism in the rear-arc (48.4–45.6 Ma) preceded the true emplacement of the Kyushu-Palau arc at 40.2 Ma, which then grew through four compositionally distinct eruptive phases until 28.8 Ma. Subsequent rollback of the Pacific slab triggered rifting of the arc (28.8–24.3 Ma) and ultimately back-arc spreading in the Shikoku and Parece Vela basins.

Plain Language Summary During 2014 International Ocean Discovery Program Expedition 351 recovered a unique ∼1,200-m-thick sedimentary and volcanic sequence at Site U1438 within the Philippine Sea Plate, which forms the upper plate of the famous Izu-Bonin-Mariana (IBM) subduction system of West Pacific. The recovered rocks recorded the beginning of the subduction, and the emplacement, growth, and death of the Kyushu-Palau volcanic arc that developed upon initiation of the IBM subduction, and may therefore hold the key to unravel the complex geological evolution of the entire West Pacific region. In this study, we reconstructed the polarity reversals of the geomagnetic field recorded at Site U1438 and produced a detailed magnetostratigraphy for this sedimentary sequence. We correlated 115 out of 142 identified magnetic reversals from our magnetostratigraphy to the reference geomagnetic polarity timescale to build a high-resolution age model of Site U1438. This age model helped us to constrain in unprecedented detail the timing of the tectonic and magmatic events that followed IBM subduction initiation at 52–50 Ma. We show that the Kyushu-Palau volcanic arc established in the upper plate 40.2 Ma, approximately 10–12 million years after the beginning of the Izu-Bonin-Mariana subduction, and then required another ∼11 million years until 28.8 Ma to grew to a full size through four compositionally distinct eruptive phases. Subsequent change in the subduction dynamics at 28.8 Ma yielded extension in the upper plate, causing the volcanic arc to split and ultimately shut down at 24.3 Ma and a new ocean basin (Shikoku and Parece Vela basins) to form within the Philippine Sea Plate.

1. Introduction

The Amami Sankaku basin (Figure 1) is the oldest part of the western Philippine Sea Plate (PSP) (Deschamps et al., 2000; Hickey-Vargas, 2005; Hilde & Chao-Shing, 1984). It witnessed the inception of the Izu-Bonin-Mariana (IBM) subduction system at 52–50 Ma (Arculus et al., 2015a; Ishizuka, Tani, et al., 2011; Reagan et al., 2010; Stern & Bloomer, 1992; Wu et al., 2016), the emplacement of new rear-arc oceanic crust at 48.7 Ma (Arculus et al., 2015a; Ishizuka et al., 2018), the subsequent building of the Kyushu-Palau volcanic arc (Brandl et al., 2017;
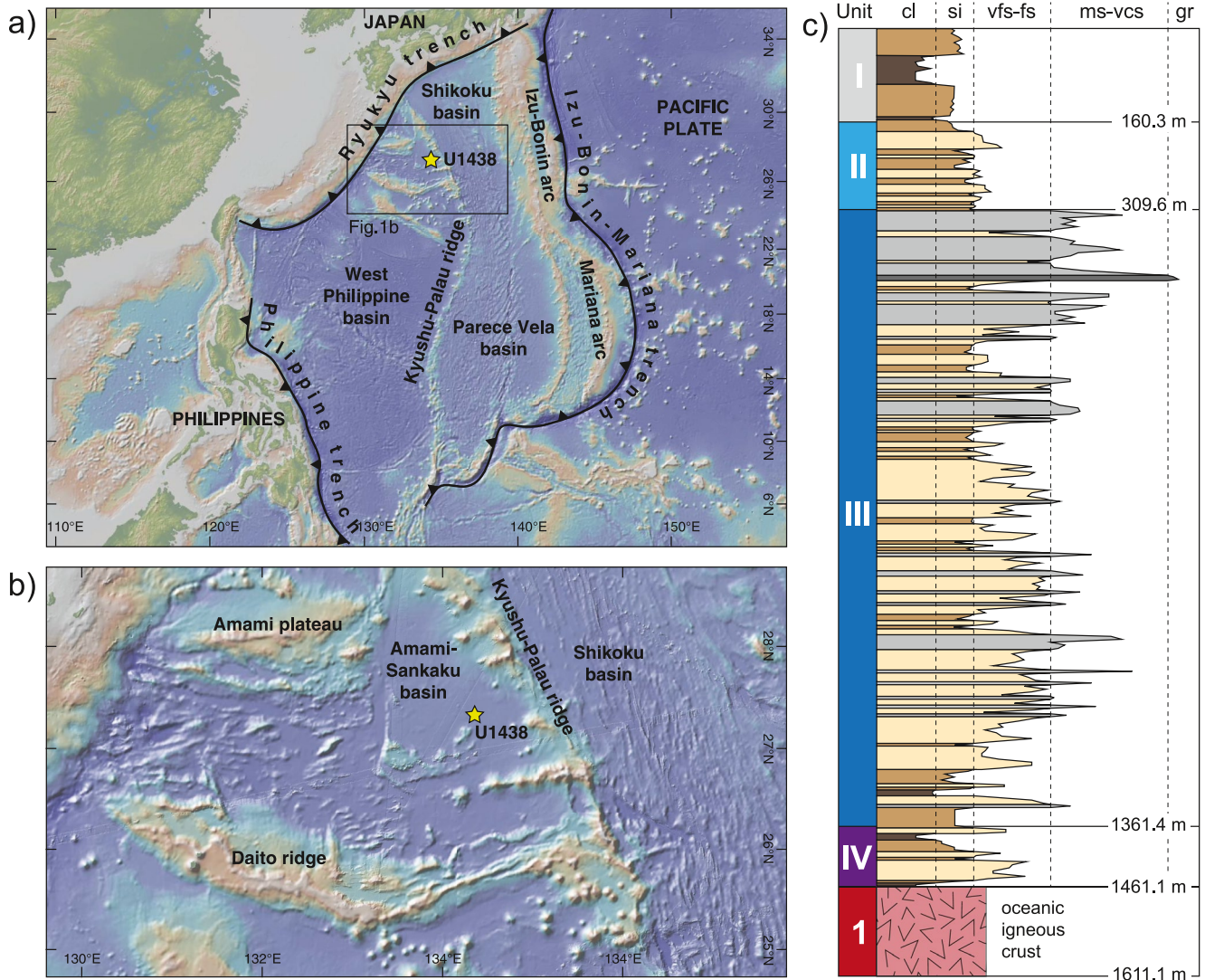
Figure 1. (a) Topographic and bathymetric map of the Philippine Sea Plate and surrounding regions (taken from GeoMapApp), showing the main tectonic structures and domains and the location of International Ocean Discovery Program Site U1438. (b) Close-up map showing the details of the bathymetry around Site U1438. (c) Lithostratigraphic log of the recovered sequence at Site U1438 from Arculus et al. (2015b). cl = clay; si = silt; vfs = very fine sand; fs = fine sand; ms = medium sand; vcs = very coarse sand; and gr = gravel.

Ishizuka, Taylor, et al., 2011; Johnson et al., 2021; Savov et al., 2006), and its ultimate demise triggered by the opening of the Shikoku and Parece Vela back-arc basins (e.g., Okino et al., 1994; Ishizuka, Taylor, et al., 2011; Okino et al., 1998).

Although known to be a first-order approximation, the precise timing of these tectonic and magmatic events in the PSP over the past ~50 Ma remains unconstrained due to the lack of a reliable and continuous geological record. In 2014, International Ocean Discovery Program (IODP) Expedition 351 recovered a unique ~1.6-km-thick sedimentary and volcanic sequence at Site U1438 (Arculus et al., 2015a, 2015b) from the northern Amami-Sankaku basin at the base of the western flank of the Kyushu-Palau Ridge (Figure 1). Sedimentary rocks at Site U1438 make up the majority of the recovered material, with a ~1.4-km thick sequence divided into four sedimentary units (Units I to IV), overlying a volcanic basement (Unit 1) (Figure 1c; Arculus et al., 2015b). Lithostratigraphic Unit I is composed of hemipelagic mud with minor ash beds, Units II and III are dominated by coarser (sand-gravel) volcaniclastic deposits, and Unit IV contains a mixed assemblage of hemipelagic and volcaniclastic sediments. Each sedimentary unit is a direct product of a specific phase of the Kyushu-Palau arc evolution, and

precise dating of this sedimentary record is therefore paramount to put the main tectono-magmatic events in the PSP into a precise temporal frame.

A preliminary age model for Site U1438 was generated during Expedition 351 shipboard operations (Arculus et al., 2015b), with a number of subsequent publications relying on it (Barth et al., 2017; Brandl et al., 2017; Johnson et al., 2021; Waldman et al., 2021). However, this preliminary age model relied on a magnetostratigraphy built using the inclinations of remanent magnetizations after a single demagnetizing step at 25 mT, rather than characteristic remanent magnetization (ChRM) directions obtained from demagnetization data using principal component analysis (Kirschvink, 1980). Furthermore, the limited time available during shipboard operations did not allow for an accurate visual inspection of the individual demagnetization plots, necessary for a reliable assessment of the magnetic polarity. Lastly, the magnetostratigraphy in Arculus et al. (2015b) did not include the bottom of the sedimentary sequence and the underlying volcanic basement.

Here, we present a new complete high-resolution magnetostratigraphy for Site U1438 based on ChRM inclinations and (where available) declinations from half core sections and discrete specimens isolated through principal component analysis. Our new age model and the calculated sedimentation rates are then used to date the tectono-magmatic events that occurred in the PSP since ~50 Ma.

2. Geological Background

2.1. Tectonic Setting

The PSP is an oceanic plate between the Eurasian, Pacific, and Australian plates, and it is surrounded by active subductions: The Izu-Bonin-Mariana trench to the east, the Ryukyu trench to the north, and the Philippine trench to the west (Figure 1).

The PSP is composed of three tectono-stratigraphic domains: (a) A western domain hosting an array of Cretaceous oceanic plateaux and ridges (including the Amami plateau and the Daito ridge) and Eocene-Oligocene basins (including the Amami-Sankaku basin), which represents the oldest part of the PSP, also known as the West Philippine Basin (Deschamps et al., 2000; Ishizuka, Taylor, et al., 2011); (b) a central domain formed by the Shikoku and Parece Vela back-arc basins (e.g., Okino et al., 1994) bounded to the west by the Eocene-Oligocene Kyushu-Palau Ridge remnant arc (Ishizuka, Taylor, et al., 2011) and to the east by the modern Izu-Bonin and Mariana arcs; and (c) an eastern domain formed by the present-day forearc and arc developed upon initiation of subduction of the Pacific plate below the PSP at ~52 Ma (Ishizuka, Taylor, et al., 2011; Reagan et al., 2010, 2015, 2019).

2.2. Stratigraphy of IODP Site U1438

During June–July 2014, IODP Expedition 351 recovered a suite of sedimentary and volcanic rocks at Site U1438 (Arculus et al., 2015b) in the Amami-Sankaku basin (27.38°N, 134.32°E; Figure 1), which is located in a rear-arc position relative to the Kyushu-Palau Ridge. Four holes were drilled (Hole U1438A, U1438B, U1438D, and U1438E), reaching a maximum depth of 1,611 m below seafloor (mbsf) and collecting a total of 1,201.39 m of cores (~75% average recovery rate). Recovered rocks consist of a thick sedimentary sequence (0–1461.1 mbsf) and the uppermost part of the oceanic crust (Figure 1b). The sedimentary sequence has been divided into four units by Arculus et al. (2015b): Unit I (0–160.3 mbsf) is an unconsolidated fine-grained hemipelagic sedimentary sequence composed of mud, tuffaceous mud, mud with ash, and clay with discrete ash beds; Unit II (160.3–309.6 mbsf) is an intercalated assemblage of medium to dark greenish gray tuffaceous mud, silt, and sand with intervening pale brown ash layers; Unit III (309.6–1361.4 mbsf) is a repetitive sequence of conglomerate- and sandstone-dominated intervals with thinner intervening mudstone-dominated intervals. The base of Unit III is transitional into Unit IV (1361.4–1461.1 mbsf), which comprises a highly diverse suite of medium to coarse sandstones, siltstones, and radiolarian-bearing mudstones, together with three thin (10–20 cm) intervals of igneous rock. Most of the sedimentary sequence is characterized by horizontal to subhorizontal beds (except for rare intervals showing tilted beds; see Figure F6 in Arculus et al. (2015b)), indicating no significant deformation at Site U1438. Below the sedimentary succession is Unit 1 (1461.1–1611.1 mbsf), which is a sparsely vesicular, microcrystalline to fine-grained, aphyric to sparsely porphyritic basalt formed upon decompressional melting of a previously depleted mantle source (Hickey-Vargas et al., 2018; Yogodzinski et al., 2018). The basalts of Unit 1 have been dated by Ishizuka et al. (2018) between 49.3 and 46.8 Ma, with a weighted average of 48.7 Ma.

3. Sampling and Methods

As part of the shipboard operations, we demagnetized a total of 1,063 archive half core sections from Holes U1438B, U1438D, and U1438E using stepwise alternating field (AF) demagnetization with the in-line coils of a 2G cryogenic magnetometer installed on the JOIDES Resolution. Three to four demagnetization steps (25, 30, 35, and 40 mT) were applied to cores from Units I, II, III, and IV, while all Unit 1 cores were demagnetized using 14 steps from 2 to 40 mT. Such a variable demagnetization pattern was adopted in response to a variable recovery rate during drilling operations. Fields above 40 mT were not applied due to a previously reported issue with the coils of the cryogenic magnetometer when working at higher fields (Arculus et al., 2015c).

Demagnetization of the archive half core sections with remanence measured at 2-cm intervals down section yielded ~60,000 demagnetization plots. Due to the great number of data and the small number of demagnetization steps, we carried out an automatic principal component analysis (PCA) using *MacPaleomag* software (written by Jeff Gee, Scripps Institution of Oceanography), where all the calculated components were anchored (e.g., Heslop & Roberts, 2016) and the NRM before demagnetization was excluded from the analysis. The use of anchored components in our PCA was a deliberate choice to enable to use the maximum angular deviation (MAD) as a proxy to discriminate ChRM components tending to the origin of the demagnetization plot axes (yielding MAD values smaller than 10°) from secondary or overprinted components not tending to the origin (yielding MAD values greater than 10°).

For the definition of the magnetic polarity, we used the inclination of the ChRMs at those intervals with MAD < 10° and the inclination of one of the AF steps (25, 35, or 40 mT) where MAD was greater than 10° upon careful visual inspection of the individual demagnetization plots. Manual principal component analysis was instead performed on all data from the igneous basement of Unit 1; hence, the magnetostratigraphy of Unit 1 entirely relies on the ChRM directions computed by PCA.

An additional 429 discrete cubic specimens (8 cm^3 volume) collected from working half core sections across the four units were demagnetized. The majority of the samples ($n = 260$) were demagnetized with AF technique, while 169 samples were subjected to thermal demagnetization. AF demagnetizations for the discrete samples were performed using 15–18 steps from 2 to 100 mT. Part of the AF-cleaned samples ($n = 47$) were demagnetized and measured during IODP Expedition 351 using an AGICO JR6A spinner magnetometer, while the remaining 213 samples were demagnetized and measured at the Fort Hoofddijk paleomagnetic laboratory (Utrecht University) with a 2G cryogenic magnetometer and built-in coils and at the PUMA paleomagnetic laboratory (University of Birmingham) with an AGICO LDA-5 demagnetizer and an AGICO JR5 spinner magnetometer. Thermal demagnetizations were carried out in 8–10 steps from 200 to 580°C or until complete demagnetization. One hundred and forty-three of the thermally cleaned samples were demagnetized during IODP Expedition 351 using an ASC Scientific thermal demagnetizer model TD-48 SC; the remaining 26 samples were demagnetized at the University of Birmingham using a Magnetic Measurements MMTD80 magnetically shielded oven. ChRM components from the discrete samples were calculated manually using *paleomagnetism.org* online software (Koymans et al., 2016).

A FlexIT orienting tool was used during the recovery of the first 19 advanced piston coring (APC) cores (i.e., B1H-B19H), providing azimuthal constraints for the top 132 core sections (0–168.9 mbsf). This allowed us to obtain both declinations and inclinations for all of Unit I and the top of Unit II.

Magnetic mineralogy was characterized using thermomagnetic experiments and the acquisition of isothermal remanent magnetization (IRM) on 15 representative samples from all lithostratigraphic units. Thermal variation of low-field (300 A/m) magnetic susceptibility was measured with an AGICO KLY4-S Kappabridge during low-temperature (−195° to 20°C using liquid nitrogen) and high-temperature (20°–700°C in argon gas) heating-cooling cycles. Curie temperatures were determined from the thermomagnetic curves using the graphical method of Petrovský and Kapička (2006). IRM was imparted with an ASC Scientific IM-10 impulse magnetizer by using 22 magnetizing steps from 10 to 1000 mT. The resulting IRM acquisition curves were analyzed using *Max Unmix* software (Maxbauer et al., 2016) to separate the different coercivity fractions (Egli, 2003a; Heslop et al., 2002; Kruiver et al., 2001).

4. Results

4.1. Magnetic Mineralogy

Results from rock magnetic experiments conducted on 15 representative samples are summarized below and grouped by lithostratigraphic unit.

Samples from the hemipelagic mudstones of Unit I show quasi-reversible thermomagnetic plots indicating no major mineralogical transformation during heating, Curie temperature of 550–560°C, and no clear Verwey transition (Figure S1 in Supporting Information S1). The IRM acquisition curve (Figure S2 in Supporting Information S1) shows that magnetic saturation was not reached at the maximum applied field of 1 T, as indicated by the gentle but progressive increase of the IRM intensity beyond 300 mT. The coercivity unmixing analysis revealed the occurrence of a predominant (94%) soft coercivity fraction (mean coercivity of 45 mT) and a minor (6%) hard fraction characterized by mean coercivity of 1512 mT (Table S1 in Supporting Information S1). Based on these results, we inferred that detrital or biogenic low-Ti titanomagnetite is the predominant magnetic carrier in Unit I, with possible occurrence of goethite in small concentrations (e.g., Dunlop & Özdemir, 1997; Egli, 2003b; Kruiver et al., 2001; Peters & Dekkers, 2003; Table S1 in Supporting Information S1).

Samples from the volcaniclastic mudstones and sandstones of Unit II show nonreversible thermomagnetic plots, indicating mineralogical transformation during heating (Figure S1 in Supporting Information S1). Two Curie temperatures of 525 and 580°C were calculated from the thermomagnetic curves, and a faint Verwey transition was observed at approximately −160°C (Figure S1 in Supporting Information S1). The IRM acquisition curve shows that magnetic saturation was reached at ~500 mT (Figure S2 in Supporting Information S1). Our coercivity unmixing analysis revealed a predominant (~90%) soft coercivity fraction with mean coercivity of ~47 mT and a minor (~10%) intermediate coercivity fraction with mean coercivities of 120–170 mT (Table S1 in Supporting Information S1). These results indicate that Unit II carries detrital or biogenic magnetite (or low-Ti titanomagnetite) and minor hematite (Table S1 in Supporting Information S1).

Samples from the volcaniclastic sandstones and mudstones from Unit III show a more variable magnetic mineralogy, with both reversible and nonreversible thermomagnetic curves and Curie temperatures of 520, 580, and 670°C (Figure S1 in Supporting Information S1). No or very faint Verwey transition was observed. Out of the two samples subjected to IRM acquisition, only one reached saturation at 200 mT (Figure S2 in Supporting Information S1). The coercivity unmixing analysis showed the occurrence of a single soft coercivity fraction (mean coercivity of 37.3 mT) in the magnetically saturated sample and a combination of soft (88%) and hard (12%) fractions, with mean coercivities of 39.6 and 1050 mT, respectively, in the nonsaturated sample. These results indicate that Unit III carries predominant detrital or biogenic (titano)magnetite and minor goethite or fine hematite (Table S1 in Supporting Information S1) (e.g., Peters & Dekkers, 2003).

Samples from the hemipelagic-volcaniclastic mudstones and sandstones of Unit IV show a partially reversible thermomagnetic curve (i.e., only between 300 and 700°C) and a poorly defined Curie temperature around 640°C (Figure S1 in Supporting Information S1). No Verwey transition was observed. A Curie temperature around 300°C can be observed in the cooling path of the thermomagnetic curve (Figure S1 in Supporting Information S1) indicating the potential formation of iron sulfides during heating (Wang et al., 2008). The IRM acquisition curve shows that saturation was never reached (Figure S2 in Supporting Information S1). The coercivity unmixing analysis revealed the occurrence of three coercivity fractions: A soft fraction (44%, with mean coercivity of 34.6 mT), interpreted as detrital or biogenic (titano)magnetite; an intermediate coercivity fraction (16%, with mean coercivity of 276.5 mT), likely represented by hematite; and a hard fraction (40%, with mean coercivity of 1205 mT), likely represented by goethite (e.g., Peters & Dekkers, 2003; Table S1 in Supporting Information S1). Although the unmixing analysis indicates a relatively complex magnetic mineralogy at these representative samples, the AF and thermal demagnetization plots from Unit IV prove the existence of intervals characterized by a simpler magnetic mineralogy carried by (titano) magnetite.

Samples from the basalts of Unit 1 show a nonreversible thermomagnetic curve, indicating mineralogical transformations during heating, a poorly defined Curie temperature of 520°C, and a well-defined Verwey transition at −160°C (Figure S1 in Supporting Information S1). The IRM acquisition curve shows that saturation was reached at approximately 100 mT (Figure S2 in Supporting Information S1). The coercivity unmixing analysis revealed a predominant (98%) occurrence of an ultrasoft fraction (mean coercivity of 14.5 mT) and a minor (2%)
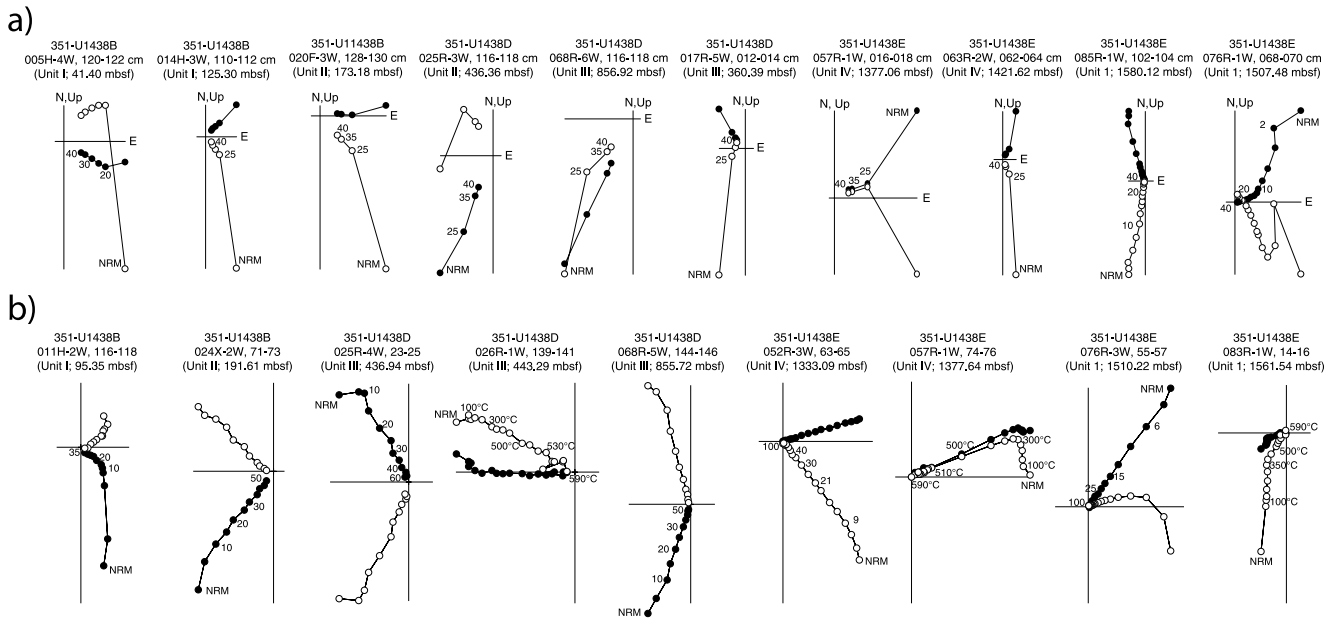
Figure 2. Representative demagnetization plots from (a) half core sections and (b) discrete specimens. Solid (open) dots are the projection on the horizontal (vertical) plane. Demagnetization steps in milliTesla (mT) or in °C are indicated in each plot.

occurrence of an intermediate fraction with mean coercivity of 609 mT. Based on these results, we conclude that the magnetic mineralogy of Unit 1 is mainly represented by pure magnetite and possible minor hematite (Table S1 in Supporting Information S1).

4.2. Stability of the Magnetic Remanence

Most of the AF demagnetization plots from half core sections show two remanence components: A high-coercivity component isolated between 25 and 40 mT, generally decaying to the origin, and a low-coercivity component, which was normally removed at 20–25 mT (Figure 2a). In several intervals of Unit III the high-coercivity component does not go to the origin of the axes and the original NRM is not fully removed, indicating the existence of a remanence carried out by high-coercivity phases that could not be removed with AF demagnetization (Figure 2a). MAD values are generally smaller than 10° and show a smaller variability in Units I, II, and IV compared to Units III and 1 (Figure S3 in Supporting Information S1). Considering that as a result of our approach MADs < 10° indicate ChRM components and MADs > 10° point out to secondary or overprinted components (see Section 3), the MAD distributions in the five lithostratigraphic units (Figure S3 in Supporting Information S1) indicate that 80% of the isolated components within each unit (except Unit III) are ChRMs; in Unit III the ChRM are only 63% of the total number of isolated components.

The common presence of a ChRM isolated within 40 mT is expected in Units I, II, and 1 due to the simpler magnetic mineralogy mainly dominated by magnetite but it is somewhat surprising in Unit IV, where a more complex magnetic mineralogy was documented. This may suggest that the overall magnetic mineralogy of Unit IV is simpler than that inferred from the rock magnetic analyses on 15 representative samples, as also suggested by the AF and thermal demagnetization plots (Figure 3a). The lower number of ChRM components in Unit III is, instead, expected due to the larger concentrations of hematite and goethite (Table S1 in Supporting Information S1), whose remanence could not been fully removed with AF demagnetization treatment.

A higher concentration of hematite and/or goethite could easily explain the partial or full overprint of the original ChRM throughout the sedimentary sequence at Hole U1438. A secondary remanence in this hard fraction can either be acquired by their authigenic growth during diagenesis of the sediment, or by drilling-induced overprint carried in primary grains of these two phases.

AF and thermal demagnetization of the discrete samples (Figure 2b) confirmed the presence of mainly two remanence components, a secondary component removed at 10–20 mT or between 100 and 350°C and a ChRM
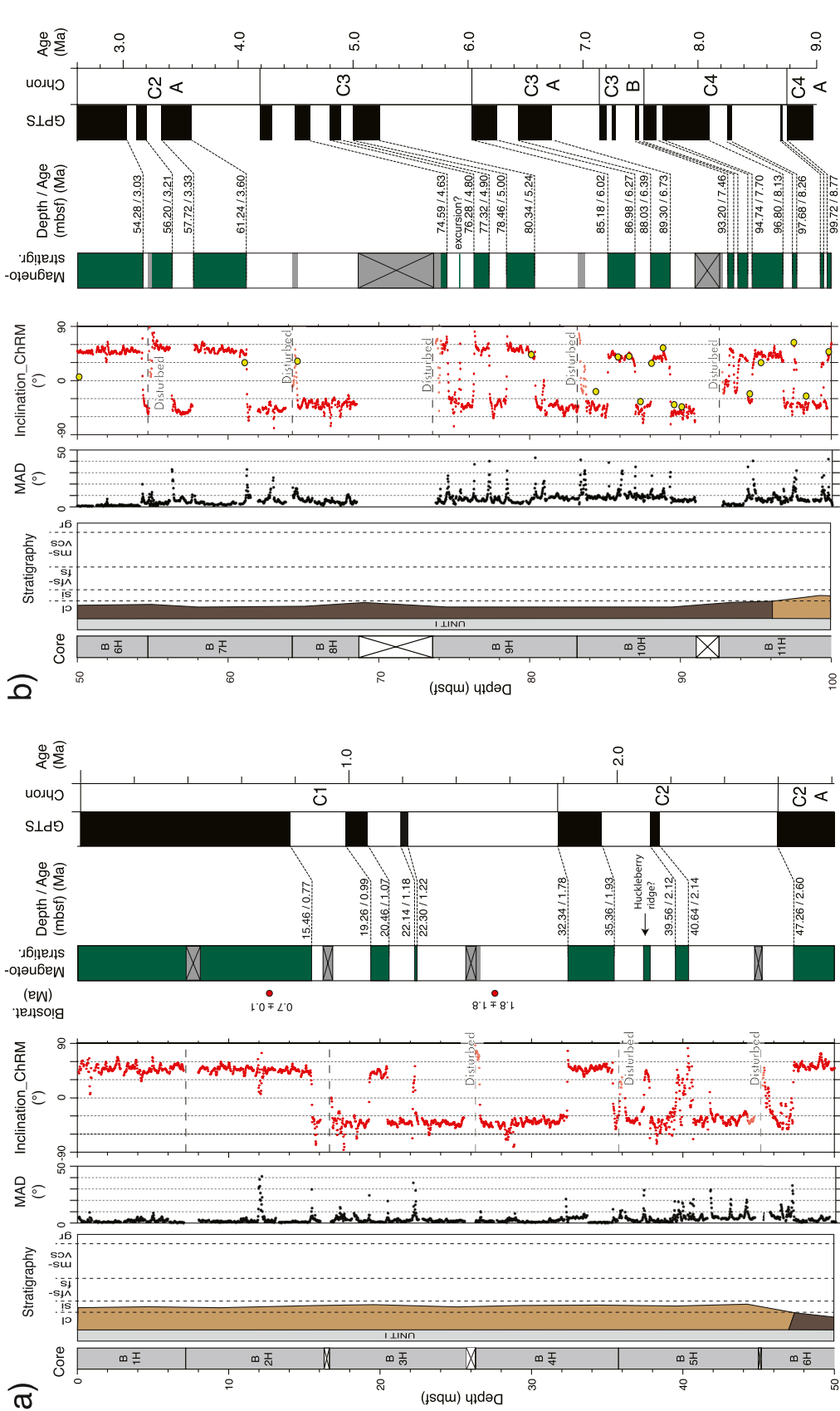
Figure 3. Magnetostratigraphy of Site U1438 for the interval (a) 0–50 mbsf, (b) 50–100 mbsf, (c) 100–150 mbsf, (d) 150–200 mbsf, (e) 200–700 mbsf, (f) 700–1200 mbsf, and (g) 1200–1600 mbsf. From left to right, each panel shows the recovery log with hole and core identification (letter = hole name; number = core number; H = advanced piston coring (APC); F = half-length APC; X = extended core barrel (XCB); and R = rotary core barrel (RCB)); a lithostratigraphic log (after Arculus et al. (2015b)) with the grain size indicated as clay (cl), silt (si), very fine sand to fine sand (vfs-fs), medium sand to very coarse sand (ms-vcs), and gravel (gr)) with the isolated anchored characteristic remanent magnetization components; the paleomagnetic inclinations of either the ChRM component or the 25 mT demagnetizing step (indicated in the plot label) from archive half core sections (red dots) and discrete samples (yellow dots); the Maximum Angular Deviation (MAD) relative to the ChRM component or the 25 mT demagnetizing step (indicated in the plot label) from archive half core sections (red dots) and discrete samples (yellow dots); the interpreted magnetostratigraphy (green = normal polarity, white = reverse polarity, and gray = undetermined polarity); and its correlation to the geomagnetic polarity timescale (GPTS) by Ogg (2020). Independent age constraints are shown to the left of the magnetostratigraphic column and are represented by foraminifers (red dots), radiolarians (blue dots), calcareous nannofossils (black dots), detrital zircon U/Pb ages by Barth et al. (2017) (green diamonds), Ar/Ar ages on amphibole by Waldman et al. (2021) (purple diamond), Ar/Ar ages on plagioclase by Ishizuka et al. (2018) (orange stars), and U/Pb zircon ages from Waldman et al. (2021) (yellow diamonds).
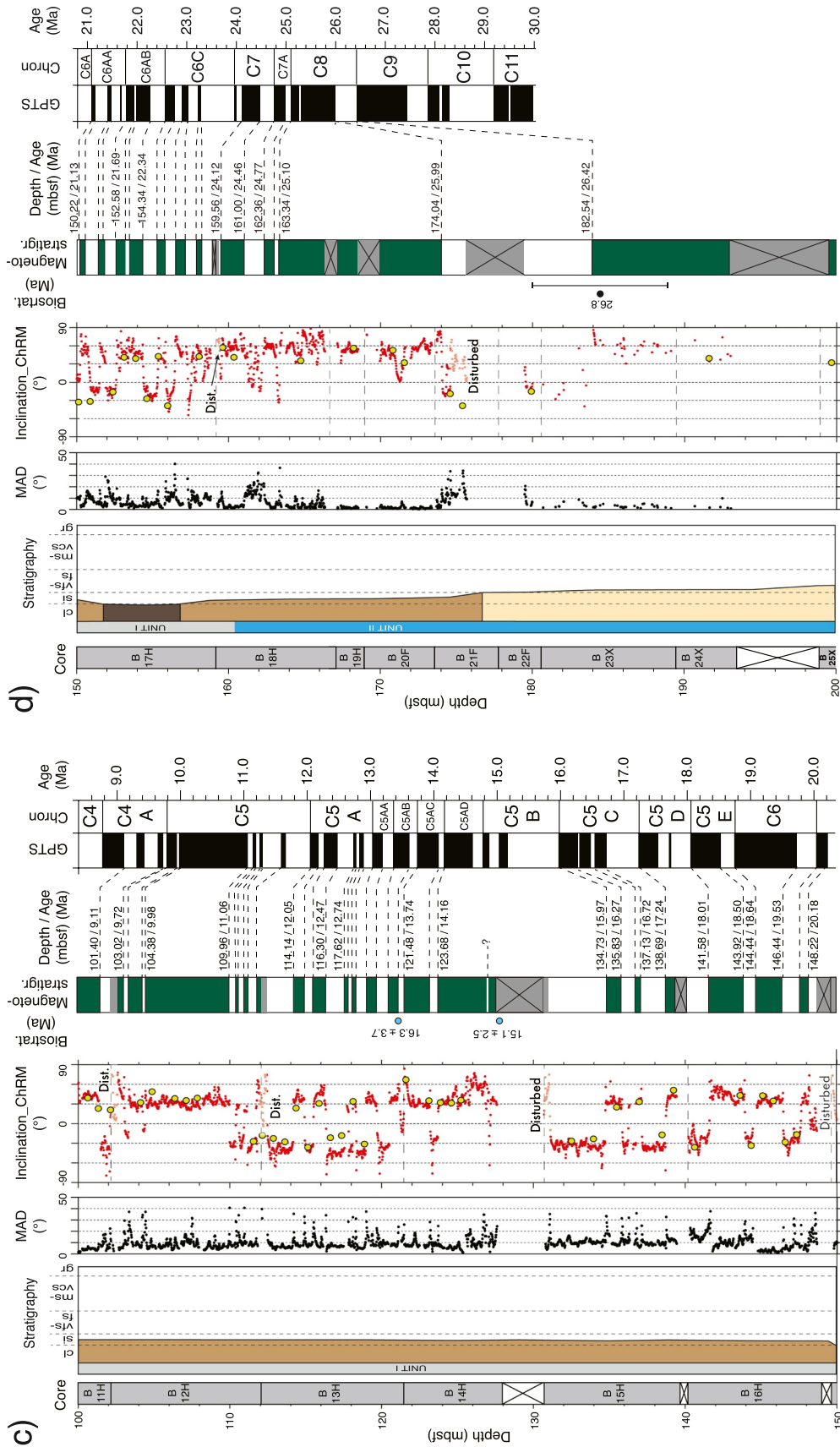
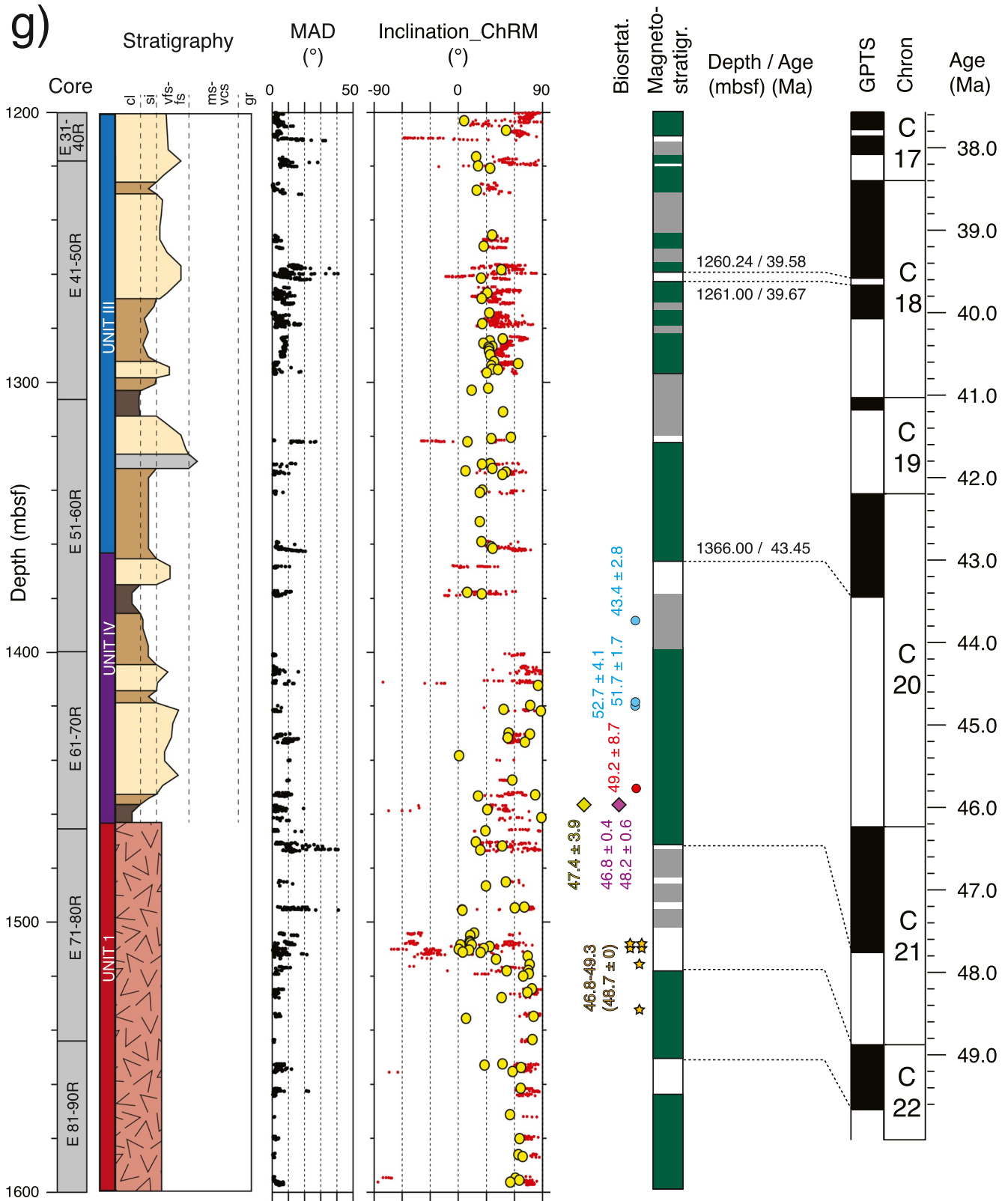**Figure 3.** (Continued)

Figure 3. (Continued)

Figure 3. (Continued)

component isolated between 20 and 100 mT or between 100–350 and 580–590°C. MAD values associated with the isolated ChRMs from the discrete samples vary between 0.1 and 28.2°, with 83% of the values being below 10° (Figure S3 in Supporting Information S1).

4.3. Paleomagnetic Directions and Magnetostratigraphy

We combined all the ChRM directions from both split-core sections and discrete samples from holes U1438B, U1438D, and U1438E and plotted their ChRM inclinations against depth in Figure 3. The inclination and, where available, declination of the individual AF steps together with the ChRMs directions are shown in Figure S4 in Supporting Information S1. Both declination and inclination show a series of downhole switches, with declination rapidly changing from northerly to southerly directions and inclinations switching from positive (i.e., down-pointing) to negative (i.e., up-pointing). The top 10–15 cm of several cores yields aberrant directions (mostly positive inclinations) associated with a high degree of core disturbance (Figure 3). This disturbance may have been caused by the fall out of sediments from the bottom of the extracted core or the borehole walls during core recovery, which were recovered at the next, deeper core where they formed a thin top layer. The data from these disturbed intervals were not considered for our magnetostratigraphy.

Positive inclinations associated with (where present) northerly declinations were interpreted as remanence acquired during normal polarity chrons, while negative inclinations with (where present) southerly declinations were interpreted as reversed polarity chrons. The switch from normal to reversed polarity (i.e., a magnetic reversal) is relatively sharp throughout most of the sedimentary sequence, with the exception of few reversals showing transitional directions and, hence, proving the high quality of the magnetic record. Remanence directions from the discrete samples are, in general, in good agreement with the polarity inferred from the half core sections (Figure 3). Localized mismatches between the half core section and discrete sample data, especially below 200 mbsf, may be explained by the lower sensitivity of the spinner magnetometer, which has been used to measure the remanence in the majority of the discrete samples.

By combining the ChRM directions from the half core sections and discrete samples from all the analyzed cores, we identified 142 reversals, providing the first high-resolution magnetostratigraphy for IODP Site U1438 (Figure 3). By integrating our magnetostratigraphy with the available biostratigraphic data (radiolarians, nannofossils, and foraminifers) from Arculus et al. (2015b), zircon U/Pb ages (Barth et al., 2017; Waldman et al., 2021), and Ar/Ar ages (Ishizuka et al., 2018; Waldman et al., 2021), we correlated 115 reversals from our magnetostratigraphy to the Geomagnetic Polarity Time Scale (GPTS) of Ogg (2020). Below, we describe our proposed magnetostratigraphic correlations in more detail for seven depth intervals, following the subdivision adopted in Figure 3.

4.3.1. Magnetostratigraphy of Interval 0–50 mbsf

In the interval 0–50 mbsf (Unit I) we identified 12 reversals based on the ChRM inclinations and declinations. These reversals are characterized by an antipodal switch of declinations (Figure S4 in Supporting Information S1), clear inclination inversions from 45° to −45°, and transitional inclinations at 9 out of 12 reversals (Figure 3a). These inclinations are close to the expected value of the geocentric axial dipole (GAD) at the latitude of Site U1438 (i.e., I = 46.3°). The MAD values are generally below 10°, except for a few intervals typically corresponding with a polarity inversion. These intermediate directions can either be a true record of the transitional directions of the geomagnetic field during a reversal or an artificial effect induced by the large response function of the sensors of the cryogenic magnetometers, which combined the opposite directions across a polarity transition into one signal. Intervals with MAD > 10° not corresponding to a magnetic reversal (i.e., at ~12 and 42–44 mbsf) may be associated with core disturbance or localized magnetic mineralogical complexities. No discrete samples were measured from this interval. The top 10–15 cm of the lower three cores of this interval (B4H, B5H, and B6H; Figure 3a) show disturbance and aberrant directions that were not considered for our magnetostratigraphy.

While the inclinations within each magnetozone show a small variation, the declinations vary more significantly, showing a typical downhole counterclockwise (CCW) rotation, which is observed at core B3H and B5H (Figure S4 in Supporting Information S1). This effect is likely related to clockwise (looking downward) rotation of the drilling barrel during piston coring and does not affect the inclinations (and therefore our magnetostratigraphy).

The reconstructed magnetostratigraphy for this interval shows a top interval from 0 to 15.45 mbsf characterized by a long normal polarity magnetozone, which we interpreted as the Brunhes chron (0–773 ka; Channell et al., 2020) in agreement with the single foraminifer datum (Figure 3a). Based on a visual approach, we correlated 10 of the 12 reversals down to the top of the Gauss chron (C2A.1n). Within the thick reverse magnetozone from 15.45 to 47.26 mbsf, which we interpreted as the Matuyama chron, we identified the Jaramillo (19.26–20.46 mbsf), Cobb Mountain (22.14–22.30 mbsf), and Olduvai (32.34–35.36 mbsf) subchrons. Two thin normal polarity intervals occur below the Olduvai subchron at ∼37–38 and ∼39–41 mbsf, with the deeper one being thicker and apparently composed of two consecutive normal polarity peaks. We correlated the deeper normal polarity interval (39.56–40.64 mbsf) to chron C2r.1n (Réunion/Feni subchron; Channell et al., 2020), in part for its longer duration and in part to keep the sedimentation rate constant. The Réunion/Feni subchron was initially thought to be composed of two distinct normal polarity intervals (Kidane et al., 1999; Mankinen & Dalrymple, 1979) but only a single interval has so far been documented in marine sediments (Channell & Guyodo, 2004; Channell & Raymo, 2003, 2016). According to our interpretation, IODP site U1438 might therefore be the first ever-documented location where sedimentary rocks recorded the Réunion/Feni subchron as two distinct normal polarity intervals. The shallower, thin normal polarity interval at 37.38–37.80 mbsf may therefore be the Huckleberry Ridge excursion (2078 ± 3 ka; Singer, 2014; Rivera et al., 2014). Although the inferred age for this excursion (2033–2051 ka) would support our interpretation, we preferred not to consider it excursion for our age model.

4.3.2. Magnetostratigraphy of Interval 50–100 mbsf

Within the interval 50–100 mbsf (Unit I), we identified 24 reversals consistently observed from both archive half core section and discrete sample data (Figure 3b). ChRM inclinations range between approximately 45° and −45°, with the top part of core B11H (Figure 3b) showing slightly shallower negative inclinations below 25°, likely resulting from deformation during APC coring (e.g., Acton et al., 2002). Declinations are antipodal across adjacent magnetozones but they do not always trend 360° or 180°, indicating a low precision of the Flex-IT orienting tool for these cores (Figure S4 in Supporting Information S1). A downhole CCW deviation of the declination is only observed in core B8H. Top core disturbance was observed in several cores and the affected data were rejected.

MAD values are generally below 10°, with larger values observed at almost every polarity transition (Figure 3b). No biostratigraphic constraints are available from this interval, and the correlation between our magnetostratigraphy and the GPTS was carried out using a visual approach. All the 24 reversals were tied to the GPTS, allowing us to identify nearly all chrons from C2An.1n down to C4An, with the exception of only a few chrons that fall within the intervals of the hole with low or no recovery (Figure 3b). We observed a very thin normal polarity interval at ∼75 mbsf, which might represent a previously unrecognized magnetic excursion occurring within chron C3n.2r and lasting, according to our age correlation 12 kyr, from 4.705 to 4.717 Ma.

4.3.3. Magnetostratigraphy of Interval 100–150 mbsf

Within the interval 100–150 mbsf (Unit I) we identified 37 reversals and one possible short excursion at ∼127 mbsf (Figure 3c) based on the ChRM inclinations. Inclinations from the discrete samples match perfectly the switch in polarity displayed by the archive half core section data. MAD values are generally below 15°, with few localized higher values at most polarity transitions and slightly higher values (up to 20°) within reverse polarity intervals. Inclinations are slightly shallower than in the above intervals, with a general distribution around 30–40° (both negative and positive polarities) and with negative inclinations generally shallower than positive inclinations. Declinations are close to either 360° or 180°, showing a higher precision of the Flex-IT tool at these cores (Figure S4 in Supporting Information S1). Only core B12H shows the previously observed downhole CCW rotation of declinations, which is even more pronounced in its top part. Top core disturbance is observed at four out of six cores (Figure 3c) and the affected data have been rejected.

Using a visual approach and considering two biostratigraphic constraints from foraminifers, we correlated all 37 reversals to the GPTS, including subchron C5r.2r-1 (Ogg, 2020), from the base of chron C4An to the base of C6An.1n, with only a few missing chrons likely falling within gaps in the recovered sequence (Figure 3c). We did not correlate the reverse polarity short interval (excursion?) at ∼127 mbsf, as there was no obvious match with the GPTS.

4.3.4. Magnetostratigraphy of Interval 150–200 mbsf

This interval contains the transition from Unit I to Unit II at 160.3 mbsf. Twenty-one reversals have been identified relying on either the ChRM inclinations and declinations or the inclinations of the remanence after 35 and/or 40 mT AF demagnetization (Figure 3d and Figure S4 in Supporting Information S1). Positive inclinations range between 45 and 60° in the 150–160 mbsf interval and then steepen downward to reach approximately 60°, with even higher values up to 90° at ~166 mbsf. MAD values for the normal magnetozones are generally below 10°. Some of the reverse magnetozones showing southerly declinations are characterized by shallow (15–30°) negative or even shallow positive inclinations (see interval 161.0–162.36 mbsf) and MAD values up to 20°. This may be caused by different factors, with the most likely being a more pervasive and not fully removed drilling overprint, as also confirmed by the steeper than expected positive inclinations; in fact, a downward vertical drilling overprint tends to steepen positive inclinations and shallow negative ones (Acton et al., 2002). This drilling overprint seems to have affected all the ferromagnetic minerals, including the sparsely occurring hard fraction (i.e., hematite and/or goethite), which we think to be the major factor responsible for preserving the drilling overprint at the maximum demagnetizing fields of 40 mT.

Declination values from archive half core sections are available down to 168 mbsf, which is the maximum depth at which the Flex-IT orienting tool was employed during coring. Below this depth (i.e., top of Unit II) the quality and amount of ChRM directions decrease sharply, inhibiting a straightforward determination of the polarity, which was established by integrating the inclinations of the ChRMs and AF steps, and additional visual inspection of the individual demagnetization plots. Core disturbance within these partially consolidated sediments further reduces the quality of the data set within this bottom interval. Nevertheless, directions from the discrete samples are consistent with those from the archive half core section data and confirm the interpreted polarity of the 21 identified reversals.

A visual correlation between our magnetostratigraphy and the GPTS, also supported by one nannofossil datum, allowed us to correlate all 21 reversals to the GPTS from C6AAn chron to C9n (Figure 3d).

4.3.5. Magnetostratigraphy of Interval 200–700 mbsf

This long interval contains the transition from Unit II to Unit III at 309.6 mbsf (Arculus et al., 2015b). Our magnetostratigraphy for this interval (Figure 3e) was built by using, on a case-by-case basis, the ChRM inclinations from half core sections and discrete samples (mainly for those intervals with MAD < 10°) or the inclinations of individual AF steps (25, 35, or 40 mT) from the archive half core sections (mainly for those intervals with MAD > 10°), unless these yielded anomalously high inclinations (Figure 3e and Figure S4 in Supporting Information S1). A careful visual inspection of the individual demagnetization plots was therefore necessary to assess the magnetic polarity, in particular for those intervals characterized by MAD values > 10° (hence potentially carrying a fully or partially overprinted ChRM). In fact, several ambiguous demagnetization plots with ChRM yielding a MAD > 10° displayed either (a) ChRM with a positive inclination but AF steps shifting to a negative inclination at higher fields (i.e., 35–40 mT) consistent with the expected values (those have typically been assigned to a reverse polarity) or (b) ChRM and 25 mT step yielding a positive inclination consistent with the expected values but negative and generally steep (>60°) inclination of the 35 and 40 mT steps (those have typically been assigned to a normal polarity). These ambiguous demagnetization plots are probably the result of ineffective removal of secondary components carried by hematite and/or goethite. This is reflected in the MAD values, which at several intervals spike from an average of 10–15° up to 40° (Figure 3e).

The majority of the ChRM inclinations range between 30 and 60° (both polarities), with several intervals showing anomalously steep positive and negative inclinations (Figure 3e). The steep inclinations are usually observed within coarse-grained intervals (Figure 3e), and may be explained by the poor ability of such lithologies to reliably preserve a stable remanence, but local drill-induced deformation can also be a viable explanation.

The ChRM directions from the discrete specimens show generally shallower, mainly positive inclinations, which are not always consistent with those from the archive half core sections. The mismatch between the archive half core section and discrete sample data may be explained by the lower sensitivity of the spinner magnetometer, mainly used to analyze these discrete samples, combined with a generally lower intensity of the remanence of these rocks. Deformation of the cubic sample during its sampling and extraction when the rock is partially or fully consolidated (i.e., below ~160 mbsf) may also be an alternative explanation of the mismatch between the archive

half core section and discrete sample data. Because of this, the inclinations from the discrete samples were not always considered for the definition of the magnetostratigraphy at this interval.

A total of 15 reversals were identified within this interval (Figure 3e). Where a gap in the data is present at a polarity transition, the magnetozone boundary was placed in the middle of the gap. Correlation between our magnetostratigraphy for this interval and the GPTS relied heavily on the biostratigraphic (foraminifers and nannofossils; Arculus et al. (2015b)) and the Pb/U detrital zircon ages by Barth et al. (2017). Nine of the 15 identified reversals were tied to the GPTS from chron C9n to C13n (Figure 3e). Out of the two normal polarity magnetozones at 466.75–477.92 and 514.96–530.00 mbsf, only the deeper one was correlated to the GPTS (chron C12n), as this provided a higher sedimentation rate that is more consistent with the overall coarser grain size of the interval above ~500 mbsf. Because the normal magnetozone at 466.75–477.92 mbsf was identified on the basis of the 25 mT inclinations only and does not show any obvious correlation with the GPTS, it is possible that this interval has a reverse polarity instead of normal (hence the question mark associated with this interval in Figure 3e). The reverse polarity magnetozone at 621–633 mbsf may correspond to the short (sub)chron within C13n, but we did not attempt a correlation here as it would have yielded an extremely high sedimentation rate at 580–620 mbsf that is not supported by the average grain size of this interval.

4.3.6. Magnetostratigraphy of Interval 700–1200 mbsf

For this interval, which falls within Unit III, we again used all the available inclinations (ChRMs and 25, 35, and 40 mT AF steps from half core sections and ChRMs from discrete samples) on a case-by-case basis to build a magnetostratigraphic log (Figure 3f).

Positive ChRM inclinations in archive half core sections exceeding 60° (both normal and reverse polarity) were interpreted as fully or partially overprinted by a drilling component and were therefore not considered for our magnetostratigraphy. At those intervals, the inclinations of the 25 mT AF step provide the most reliable polarity constraint. The cause for the steep negative inclinations like those observed at ~920–940 mbsf obviously cannot be a drilling overprint, so perhaps these anomalous inclinations are due to local deformation or magnetic mineralogical complexities.

Below 900–1000 mbsf, both the ChRM and 25 mT AF step inclinations are anomalously steep (mainly positive), and the polarities were established using mainly the 35 and 40 mT AF steps, which range between 30 and 60° at both normal and reverse polarities (Figure 3f and Figure S4 in Supporting Information S1). MAD values are generally lower than 10–15° but they increase up to 40° mainly within the reverse magnetozones, likely due to a not fully removed drilling overprint.

ChRM inclinations from discrete specimens are always shallower than the ChRMs from the half core sections, especially within the interpreted reverse magnetozones, where these do not always switch to negative values, but rather show very shallow inclinations difficult to interpret for the definition of the polarity.

We identified in this interval 25 reversals, plus six thin, poorly defined reverse magnetozones. Using the three biostratigraphic (nannofossil) and three detrital zircon data, we correlated 11 of the 25 reversals to the GPTS from chron C15n to C18n (Figure 3f), while we did not find an obvious way to correlate the six thin reverse magnetozones.

4.3.7. Magnetostratigraphy of Interval 1200–1600 mbsf

This interval comprises the three bottom lithostratigraphic units: The sedimentary Unit III and Unit IV and the volcanic Unit 1. The ChRM inclinations from the archive half core sections are predominantly positive and ranging from 30° to 60°; however, several intervals show inclinations steeper than 60°, suggesting a pervasive drilling overprint (Figure 3g). The majority of these steep inclinations occur in Unit 1, although they are also abundant in Unit IV, while they only occasionally occur in Unit III. Altogether the data from this interval do not provide a continuous magnetostratigraphy due to a poor recovery rate of the cores and an inefficient preservation of the remanence. The inclinations from the discrete specimens are all positive, ranging from 0 to 90°, and showing a downhole variation consistent with the archive half core section data (Figure 3g).

The interpreted polarity of this interval is mainly normal, with various thin reversely magnetized intervals occurring at various depths and one thicker at the top of Unit 1, which allowed us to identify eight potential reversals (Figure 3g). The quality and amount of the data in this interval are not ideal and the overall reliability of this part

of the magnetostratigraphy is low. Independent age constraints for this interval are provided by radiolarian and foraminifer determinations from Unit IV (Arculus et al., 2015b), Ar/Ar and U/Pb ages from Unit IV (Waldman et al., 2021), and Ar/Ar ages from Unit 1 (Ishizuka et al., 2018). The biostratigraphic ages have a large uncertainty and their vertical distribution seems to indicate reworking, with two data older than the underlying volcanic basement. The Ar/Ar and U/Pb ages of Waldman et al. (2021) from the base of Unit IV are consistent with a correlation of the base of Unit IV to chron C21n. We then tentatively correlated the thin reverse magnetozone at ~1,260 mbsf to chron C18n.1r and the reversal at 1,366 mbsf to the base of chron C20n.

Unit 1 was dated by Ishizuka et al. (2018) using six samples from 1,509 to 1,534 mbsf, which yielded ages ranging from 46.8 to 49.3 Ma, with a weighted average of 48.7 Ma. For our final age model, we assigned this weighted average age to the top of Unit 1 at 1461.1 mbsf. The reversely magnetized interval occurring at the top of Unit 1 may indeed correspond to chron C21r, while the possible reversal at 1550–1560 mbsf could suggest an older age of deeper portions of Unit 1; however, due to the potential intrusive nature of some intervals of this unit (Arculus et al., 2015b), we did not correlate these reversals to the GPTS.

4.4. Age Model of IODP Site U1438

Our magnetostratigraphic analysis of the sedimentary sequence at IODP Site U1438 provided 115 age-depth constraints (Table S2) that we used to build a high-resolution age model (Figure 4). This has a high resolution for the uppermost 160 m of the sequence (i.e., Unit I), where it is based on 86 dated reversals (i.e., 75% of the total amount of data) and supported by five biostratigraphic ages. This interval covers approximately half of the time of the entire sedimentary sequence. The dating of the remaining ~1,300 m of the sedimentary sequence relies on 29 dated reversals and a large number of independent age constraints, including 14 biostratigraphic data (foraminifers, calcareous nannofossils, and radiolarians), nine U/Pb zircon ages from Barth et al. (2017) and Waldman et al. (2021), and two Ar/Ar ages from Waldman et al. (2021).

The age for the bottom part of the sedimentary sequence was determined by connecting the weighted average age of the basement (i.e., 48.7 Ma) to the last magnetostratigraphic constraints in Unit III at 1,366 mbsf (Figure 4). All the other independent age constraints, excluding the two reworked radiolarian data, support our interpreted age for this bottom interval.

Our age model indicates that a complete sedimentary sequence is preserved at IODP Site U1438, which recorded the geological evolution of this region since the emplacement of lavas erupted in a rear-arc setting at 48.7 Ma. The implications of the ages inferred for the various stratigraphic intervals will be discussed in Section 5.

Three distinct segments with different slopes can be identified in our age model (Figure 4): A shallow segment at the top (0–163.34 mbsf), including Unit I and the top of Unit II, a steep segment in the middle (164.34–1,209.36 mbsf), comprising Unit II and Unit III, and a moderately steep segment at the bottom (1,209.36–1,461.08 mbsf), comprising the bottom part of Unit III and Unit IV. This pattern, which indicates two distinct times when sedimentation rates abruptly changed, mirrors the downhole variation of lithologies and their grain size distributions, with the top interval composed of the finest lithologies (i.e., mudstones and siltstones), the middle interval predominantly dominated by fine to coarse sand and gravel, and the bottom interval dominated by siltstones and fine sand (Figure 4).

4.5. Sedimentation Rates

Our magnetostratigraphy-based age model allowed precise determination of sedimentation rates throughout the entire sedimentary sequence. To take into account the effect of compaction on the sedimentation rates, we computed the decompacted thickness of the sediments using their porosity, following the method of Van Hinte (1978) and recalculated corrected sedimentation rates using the decompacted thicknesses of each interval following the approach used by McNeill et al. (2019) and subsequently Maffione and Herrero-Bervera (2022). Van Hinte (1978) proposed that the initial thickness of a sedimentary unit at the time of deposition and any time thereafter is controlled by the change in porosity of the sediment during burial; in fact, during burial-induced compaction, the volume of the pore space decreases, while that of the grains remains fixed. So, in other words, the variation of thickness during burial is a direct function of the change in porosity. This conclusion, however, assumes that there is no dissolution or cementation during burial, which clearly cannot be ruled out in the studied
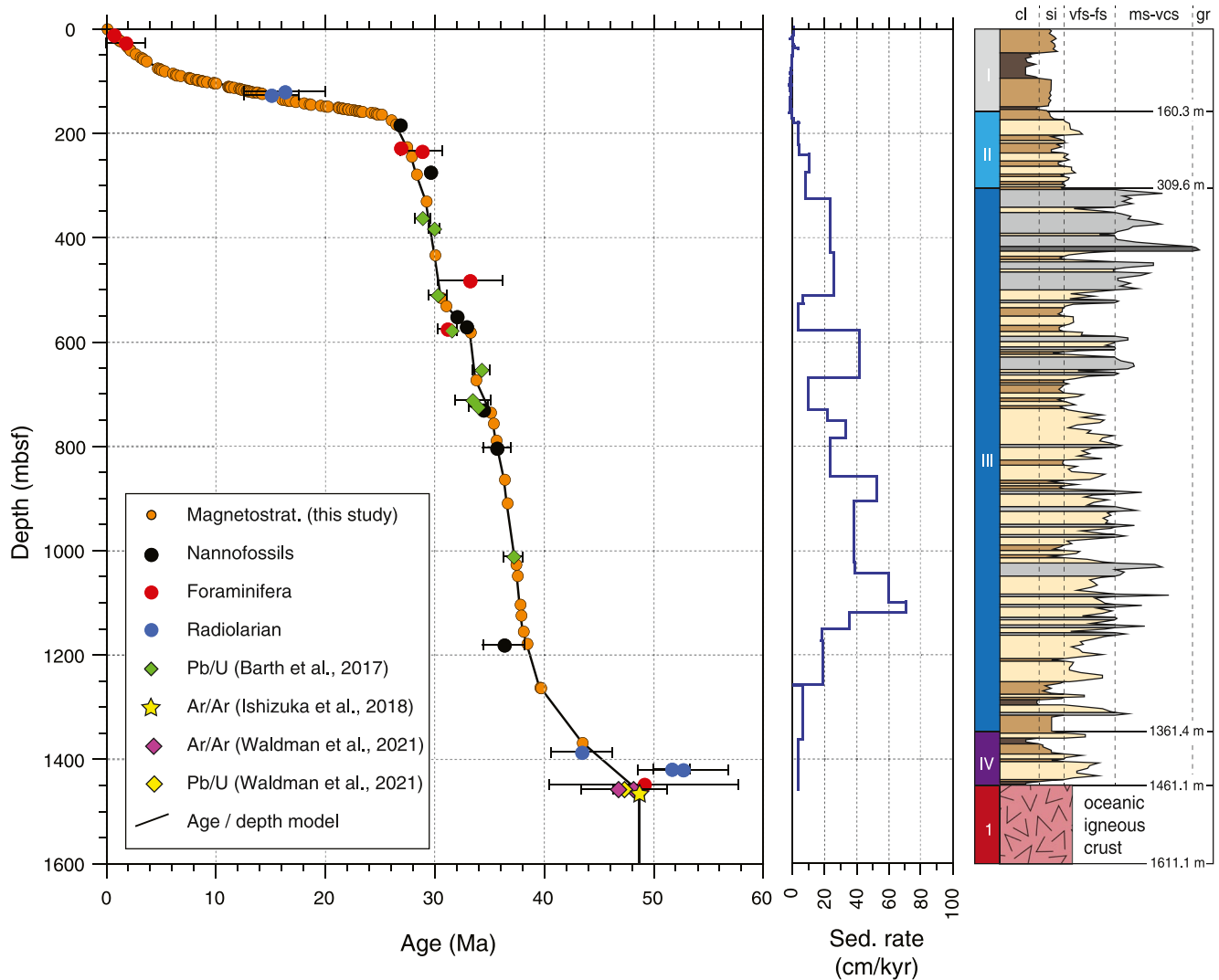
Figure 4. (Left) Age/depth model obtained from the magnetostratigraphic ages; (center) sedimentation rates calculated after decompaction (see text); (right) Lithostratigraphic log of Ste U1438 after Arculus et al. (2015b).

sediments, and may therefore provide an additional source of error in the calculation of the sedimentation rates. Also, compaction of fine-grained lithologies (clay and silt) may operate differently, as also documented in Unit I by Maffione and Morris (2017), and this may provide a further source of error in the calculations.

According to Van Hinte (1978), the decompacted thicknesses can be calculated by the formula below:

$$T_D = \frac{T_i \left(1 - \phi_i\right)}{\left(1 - \phi_i^*\right)}$$

where T_i and ϕ_i are the thickness and average porosity, respectively, for a given interval, and ϕ_i^* is the initial porosity of the sediment at the sea floor.

In our calculation, the measured porosity (ϕ_i) was not the raw porosity value at a given interval but a value extrapolated from a porosity function. To build the porosity function we first applied a second order polynomial best fit on the porosity values obtained from the moisture and density measurements on discrete samples performed during IODP Expedition 351 operations (Table S3). We rejected the data yielding residuals higher than 10% (in porosity values) and then fitted a 30th order polynomial to the remaining points. The initial porosity (ϕ_i^*) at Hole U1438 was extrapolated from the porosity function at 0 mbsf, which provided a value of 0.7566 (Table S3).

Using the above equation, we calculated the decompacted thickness for each interval between two adjacent tie points of the reconstructed age model. From the decompacted thickness for each interval, we then calculated new corrected values of sedimentation rates (Table S2).

The corrected sedimentation rates show a general increase downhole from Unit I to Unit II and then Unit III, with average values of 0.8, 3.5, and 29.7 cm/kyr on average, respectively, and then decrease in Unit IV where the average sedimentation rate is 7.1 cm/kyr. The downhole variation of the computed sedimentation rates is in excellent agreement with the lithology and grain size distribution, with Unit I and Unit III showing the finest and coarsest average grain size and the slowest and fastest accumulation rates, respectively. The good match between sedimentation rates and grain size is also observed at the small scale across layers of different grain sizes within each lithostratigraphic unit (Figure 3).

Extremely high sedimentation rates up to 72.5 cm/kyr can be observed in Unit III at 1,050–1,150 mbsf. While these values are close to those documented from other volcanic arcs (e.g., Watt et al., 2012), they are surprisingly higher than those from the top part of the Unit III at ∼300–500 mbsf, where the coarsest average grain size is observed (Figure 4). This may indicate that the coarser grain size at the top part of Unit III is not indicative of a higher accumulation rate but probably only of a closer source (i.e., a new volcanic edifice formed close to Site U1438).

5. Discussion

Our magnetostratigraphic analysis and the inferred age and sedimentation rates of the hemipelagic and volcaniclastic sediments recovered at IODP Site U1438 within the Amami-Sankaku basin (Figure 1) provide a unique opportunity to constrain the timing of the growth and demise of the Kyushu-Palau volcanic arc, associated with the initiation of the Izu-Bonin-Mariana subduction, and subsequent rifting and back-arc spreading at the Shikoku and Parece Vela basins. The magnetostratigraphy proposed here builds on top of the preliminary study presented in Arculus et al. (2015b), but shows five major differences and improvements: (a) The preliminary magnetostratigraphy in Arculus et al. (2015a, 2015b, 2015c) reached a maximum depth of 846 mbsf and did not include the results from the bottom two lithostratigraphic units (IV and 1), while this study presents the magnetostratigraphy of the entire drilled sequence down to 1,600 mbsf, including Unit IV and Unit 1, making it one of the longest magnetostratigraphic logs ever produced from IODP cores; (b) this study documented 115 reversals, against the 87 of the preliminary study; (c) the occurrence and depth of 55 out of the 87 previously identified reversals (i.e., 65%) have been reassessed and amended based on a more detailed analysis of the demagnetization diagrams; (d) the age of all reversals have been updated using the more recent timescale of Ogg (2020); and (e) in this study, we performed a full principal component analysis providing new ChRM inclinations and used the MAD values combined with a visual inspection of the demagnetization plots to determine on a case-by-case basis the magnetic polarity of the studied rocks.

In the next sections, we discuss the results from the five lithostratigraphic units recovered at Site U1438 from older to younger and the implications for the tectono-magmatic evolution of the Philippine Sea Plate since ∼50 Ma (Figure 5).

5.1. Unit 1: Upper Plate Crustal Accretion Upon Subduction Initiation

Lithostratigraphic Unit 1 (1,461.1–1,611.1 mbsf) represents the top part of the volcanic crust emplaced in the young IBM rear-arc as a response to subduction initiation at 52–50 Ma (e.g., Ishizuka et al., 2018). These volcanic rocks are an ultradepleted MORB variety (Hickey-Vargas et al., 2018; Yogodzinski et al., 2018) compositionally similar to forearc basalts (FAB) occurring in the modern IBM forearc (Ishizuka, Tani, et al., 2011; Reagan et al., 2010). The magnetic remanence of this unit seems to have been heavily affected by a drilling overprint, and although the computed magnetozones (Figure 3) are consistent with the established age of the crust, for the dating of Unit 1, we relied exclusively on the radiometric dating by Ishizuka et al. (2018), which indicates an emplacement age of 48.7 Ma.

Because these volcanic rocks were emplaced 50–80 km west (in present-day coordinates) of the future Kyushu-Palau arc (hence in a rear-arc position) and about 250 km west of the active trench, their origin has been associated with an extremely diffuse rear-arc extension occurring soon after the emplacement of FABs in the forearc (Arculus et al., 2015a) (Figures 5a and 5b).
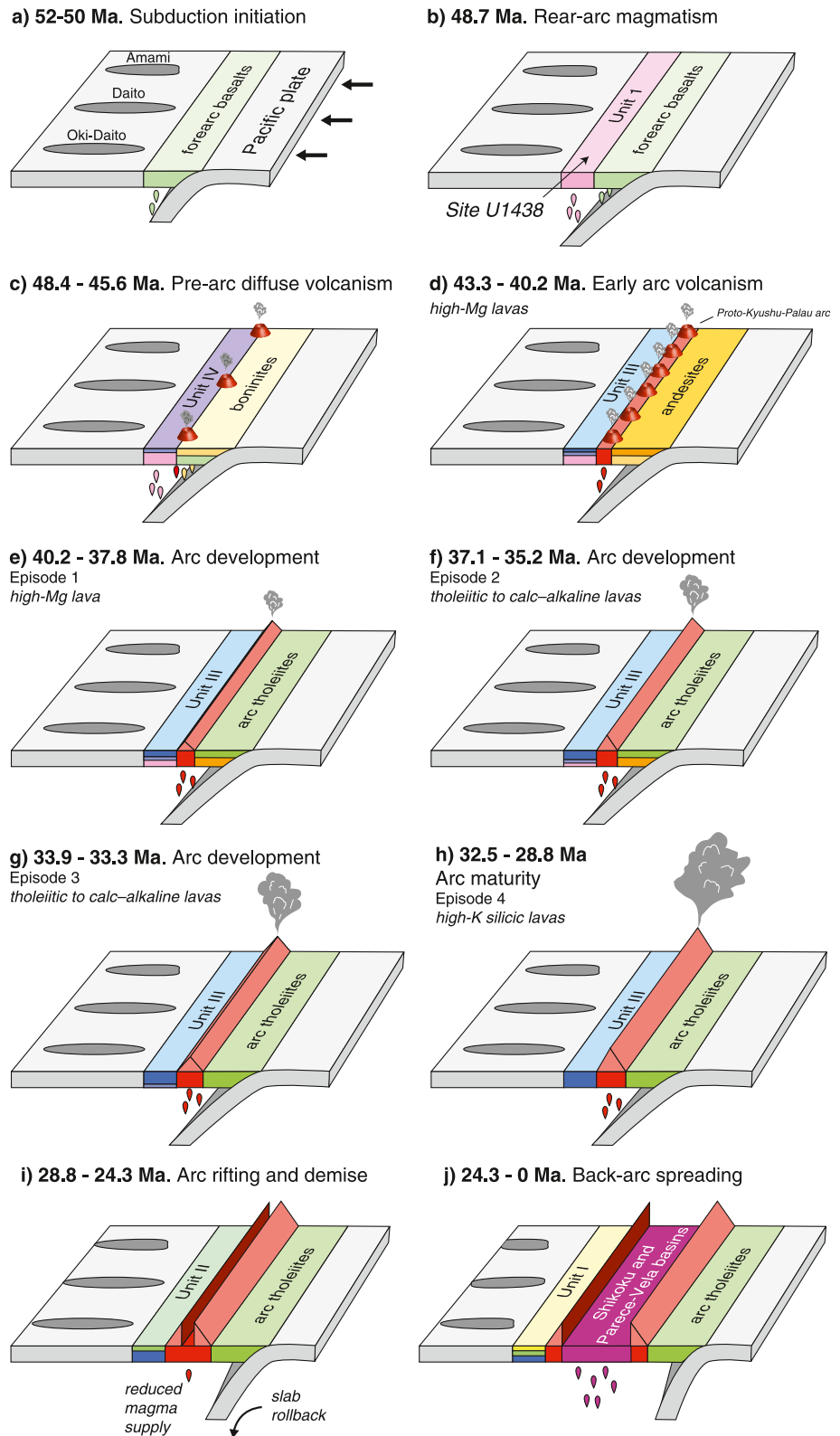
a) 52-50 Ma. Subduction initiation

b) 48.7 Ma. Rear-arc magmatism

c) 48.4 - 45.6 Ma. Pre-arc diffuse volcanism

d) 43.3 - 40.2 Ma. Early arc volcanism
high-Mg lavas

e) 40.2 - 37.8 Ma. Arc development
Episode 1
high-Mg lava

f) 37.1 - 35.2 Ma. Arc development
Episode 2
tholeiitic to calc–alkaline lavas

g) 33.9 - 33.3 Ma. Arc development
Episode 3
tholeiitic to calc–alkaline lavas

h) 32.5 - 28.8 Ma
Arc maturity
Episode 4
high-K silicic lavas

i) 28.8 - 24.3 Ma. Arc rifting and demise

j) 24.3 - 0 Ma. Back-arc spreading

Figure 5.

5.2. Unit IV: Prearc Magmatic Activity

Lithostratigraphic Unit IV (1,361.4–1,461.1 mbsf) is the first sedimentary unit deposited above the volcanic basement (Unit 1) and forms the base of the thick volcaniclastic succession recovered at Site U1438. Its boundary with volcanic Unit 1 is abrupt but the occurrence of a few intervals of volcanic rocks at its base (Waldman et al., 2021) as well as local hydrothermal alteration (Arculus et al., 2015b) suggests that Unit IV was deposited above the volcanic basement immediately after its emplacement to the seafloor at 48.7 Ma.

Waldman et al. (2021) divided Unit IV into three subunits based on changes in lithology, modal sediment composition, and bedding style: Subunit IVc (1,461.1–1,456.3 mbsf) represented by pelagic mudstones; subunit IVb (1,456.3–1,404.9 mbsf) composed of an alternation of volcaniclastic sandstones, siltstones, and conglomerates exhibiting a Bouma sequence with pelagic mudstones, intercalated by three thin basaltic andesite layers; and subunit IVa (1,404.9–1,359.6 mbsf) containing mudstone with minor volcanic sandstone.

Only one magnetostratigraphic age could be determined from the top part of Unit IV (Figure 3), which is consistent (within error) with the radiolarian age from a slightly deeper interval. Similarly, the Ar/Ar amphibole ages of 46.8 ± 0.4 and 48.2 ± 0.6 Ma and a U/Pb zircon age of 47.4 ± 3.9 Ma from the base of Unit IV (i.e., subunit IVc; Waldman et al., 2021) are consistent with the age of the underlying volcanic basement. The age of Unit IV was calculated by interpolation using the age of Unit 1 (48.7 Ma at 1461.1 mbsf) and the magnetostratigraphic age toward its top (43.45 Ma at 1,366 mbsf; Figure 4 and Table S2). Based on our age model Unit IV was deposited over 5.3 Myr, between 48.6 and 43.3 Ma.

The average sedimentation rate of 7.1 cm/kyr calculated for Unit IV (Figure 4 and Table S2) does not take into account the small-scale variability associated with the alternation of coarse- and fine-grained intervals across its top, center, and base, corresponding to subunits IVa, IVb, and IVc, respectively, following the classification by Waldman et al. (2021). Higher sedimentation rates are, in fact, expected in subunit IVb, which shows the coarsest grain size within Unit IV. According to Waldman et al. (2021), subunit IVb represents the product of early upper plate volcanism at minor unidentified volcanic centers following an initial period of deep-marine pelagic sedimentation (subunit IVc). The exact provenance of these deposits is uncertain and they might have been sourced either from the Daito region further to the west (Waldman et al., 2021) or by the nascent Kyushu-Palau arc (Johnson et al., 2021). Volcaniclastic turbiditic deposits occurring at the top of Unit IV (i.e., subunit IVa) show a lower energy and mark, therefore, a pause between the prearc (subnit IVb) and the early arc (base of Unit III) volcanic activity of the Kyushu-Palau arc (Waldman et al., 2021). We now can bracket this prearc diffuse magmatic activity in the rear-arc between 48.4 and 45.6 Ma, which is therefore concomitant with the emplacement of boninites in the forearc (48-46 Ma; Ishizuka, Tani, et al., 2011) (Figure 5c).

5.3. Unit III: Emplacement and Growth of the Kyushu-Palau Arc

Unit III (309.6–1361.4 mbsf) is the thickest of the four sedimentary units and the one with the coarsest average grain size (i.e., conglomerate and sandstone intervals with sparse thin pelagic mudstone intervals). This unit comprises a sequence of volcaniclastic gravity-flow deposits supplied by submarine channels branching from the Kyushu-Palau arc located ~80 km to the east and sourced by subaerial to submarine eruptions (pyroclastics), sector collapse, anderosion of subaerial volcanic edifices (epiclastics) (Johnson et al., 2021).

Figure 5. Tectono-magmatic evolution of the Izu-Bonin-Mariana forearc and rear-arc region since 52–50 Ma, based on our new magnetostratigraphic data combined with previous results from stratigraphy (Johnson et al., 2021; Waldman et al., 2021), geochemistry (Brandl et al., 2017), and geochronology (Ishizuka et al., 2018). (a) Subduction initiation occurs at ~52–50 Ma, leading to the emplacement of forearc basalts (FABs) in the proximity of the active trench. (b) Following forearc extension during subduction initiation, diffuse magmatism occurs in the rear-arc region where FAB-affinity lavas are deposited at IODP Site U1438 (Unit 1). (c) Before the rising of the Kyushu-Palau volcanic arc sparse magmatism occurred in the rear-arc, with high-Mg products recorded within Unit IV, while boninites were being erupted in the forearc. (d) Early activity of the proto–Kyushu-Palau arc occurred before the true growth of the arc and was characterized by high-Mg products erupted and deposited in the rear-arc as Unit III, while andesites were being erupted in the forearc. (e, f, g, and h) The growth of the Kyushu-Palau arc occurred through four distinct eruptive phases called "Episodes" (Johnson et al., 2021) characterized by a shift from high-Mg to tholeiitic to calc-alkaline melts. Episode 4 represents the arc's full maturity, which was marked by an increase of materials erupted and a shift to high-K melts. (i) The beginning of rollback of the Pacific slab led to rifting of the volcanic arc at 28.8 Ma and an abrupt decrease of the volcanic activity, which continued sporadically until 24.3 Ma during deposition of Unit II. (j) Back-arc spreading in the Shikoku and Parece Vela basins started at 24.3 Ma and since then the rear-arc domain hosted pelagic sedimentation (Unit I) characterized by deposition of discrete ash layers sourced by nearby volcanic arcs of Japan and the Philippines.

Despite the nonideal lithology for paleomagnetic analysis (i.e., coarse-grained turbidite flows), several intervals of this unit, perhaps those with the finest grain size, yield a primary remanence. This allowed us to date 19 reversals within Unit III, which together with the biostratigraphic (Arculus et al., 2015b) and U/Pb zircon (Barth et al., 2017) revealed that Unit III have been deposited over ~14.5 Myr between 43.3 and 28.8 Ma (Figure 4; Table S2).

Sedimentation rates for Unit III are the highest of the entire sequence, reaching values as high as 72.5 cm/kyr (Table S2; Figure 4). The base of Unit III records the first abrupt increase of sedimentation rates, which spike from 7.1 cm/kyr on average in Unit IV and base of Unit III to over 20 cm/kyr at ~1,260 mbsf. The increase of sedimentation rates at this depth matches very well with the emplacement of the Kyushu-Palau arc identified in Unit III at 1,275 mbsf by Johnson et al. (2021). We therefore dated the deposition of the lowermost portion of Unit III (1,361–1,275 mbsf) characterized by low sedimentation rates to 43.3–40.2 Ma (Figure 4; Table S2). This stratigraphic interval recorded the stage of early arc magmatism of the proto-Kyushu-Palau arc (Figure 5d), which was characterized by high-Mg andesitic melts (Brandl et al., 2017) emplaced in the rear-arc synchronously with the transition from boninitic to arc tholeiitic and calc-alkalic lavas in the forearc region (Ishizuka, Tani, et al., 2011). This implies that the Kyushu-Palau arc fully established 8.5 Myr after rear-arc extension and emplacement of new volcanic crust (Unit 1) at 48.7 Ma, and about 10–12 Myr after the beginning of the IBM subduction (Figures 5a and 5b).

The development of the Kyushu-Palau arc was divided by Johnson et al. (2021) into four phases, termed as "Episodes," identified in Unit III based on allocyclic changes (pulses) in sediment supply resulting from the tempo of magmatic processes: Episode 1 (1,025–1,275 mbsf), Episode 2 (740–980 mbsf), Episode 3 (590–680 mbsf), and Episode 4 (310–565 mbsf). These volcanic episodes have a distinct geochemical signature, with Episode 1 containing the early high-Mg andesitic products, Episodes 2 and 3 showing an intermediate calc-alkaline to tholeiitic composition, and Episode 4 dominated by the high-K silicic products of a mature arc (Brandl et al., 2017; Johnson et al., 2021). The distribution of the sedimentation rates calculated in this study supports this subdivision, with a broad peak in correspondence of Episodes 1 and 2 and two discrete peaks observed at the depths of Episodes 3 and 4 suggested by Johnson et al. (2021).

We dated these four eruptive phases that contributed to the growth of the Kyushu-Palau arc to 40.2–37.8 (Episode 1; Figure 5e), 37.1–35.2 (Episode 2; Figure 5f), 33.9–33.3 (Episode 3; Figure 5g), and 32.5–28.8 (Episode 4; Figure 5h) Ma. The duration of each eruptive periods at Site U1438 (i.e., 0.6–3.7 Myr) is higher than that recorded at the Kamchatka and Aleutian arcs, which is in the order of 0.1–0.3 Myr (Prueher & Rea, 2001), but is close to the average lifespan of individual volcanic edifices documented from the Lesser Antilles island arc (e.g., Harford et al., 2002; Watt et al., 2012). Episode 4 is characterized by the highest average grain size, which may indicate the emergence of a more proximal volcanic edifice just prior to the demise of the arc (Johnson et al., 2021).

5.4. Unit II: Demise of the Kyushu-Palau Arc and the Opening of the Shikoku and Parece Vela Back-Arc Basins

Unit II (160.3–309.6 mbsf) is composed of a repetition of tuffaceous mudstones, siltstones, and sandstones with intercalated ash layers, likely sourced from a combination of gravity flow and air fall volcanic deposits and pelagic muds (Arculus et al., 2015b). The age of Unit II relies on nine dated reversals (Table S2), which reveal a deposition between 28.8 and 24.3 Ma (Figure 4, Table S2). Sedimentation rates show a three-fold up-section decrease in sedimentation rate, from ~30 to ~10 cm/kyr at the Unit III-Unit II transition, followed by a progressive decreasing to 0.5 cm/kyr toward the top of Unit II (Figure 4; Table S2).

In agreement with previous models (Ishizuka, Tani, et al., 2011; Johnson et al., 2021), we interpret the sharp decrease in sediment supply and grain size at the Unit II-III boundary as the end of the main volcanic activity at the Kyushu-Palau arc. The demise of the Kyushu-Palau arc is thought to have been caused by its rifting triggered by slab rollback of the Pacific lithosphere, which ultimately led to back-arc spreading of the Shikuku and Parece Vela basin further to the east (Figure 5i). According to previous works on marine magnetic anomalies from these back-arc basins, rifting of the Kyushu-Palau arc started at ~30 Ma (Okino et al., 1999) and was followed by back-arc spreading between 27 and 15 Ma (Kasuga & Ohara, 1997; Okino et al., 1994, 1998, 1999). Lavas erupted at the Kyushu-Palau arc at 28–25 Ma (Ishizuka, Taylor, et al., 2011) would imply a longer activity of the Kyushu-Palau arc and a delayed beginning of rifting at 25 Ma. The product of the latest magmatic activity at the Kyushu-Palau arc may be represented by the fine-to very fine-sand turbiditic layers of Unit II. However, we

cannot ignore the abrupt decrease of sedimentation rates and grain size of sediments at the Unit III-II transition at 28.8 Ma. To combine all the existing evidence into a unifying model, we propose that rifting of the Kyushu-Palau arc occurred at a very slow rate over 4–5 Myr from 28.8 to 24.3 Ma, causing a sharp decrease of the magmatic activity, while still allowing the dying arc to produce eruptions that became sparser and less powerful over time from 28.8 to 24.3 Ma when they eventually ceased altogether (Figure 5i). The suggested cessation of volcanism at the Kyushu-Palau arc at 24.3 seems to be in excellent agreement with the initial true seafloor spreading in the Shikoku Basin (which is located adjacent to Site U1438) at ∼22.5 Ma (Chron C6Br) documented by Okino et al. (1999), providing an even stronger support to our magnetostratigraphy and age model at Site U1438.

5.5. Unit I: Rear-Arc Pelagic Sedimentation

Lithostratigraphic Unit I (0–160.3 mbsf) is a postarc deposit consisting of a range of fine-grained sediments from pelagic and hemipelagic to volcaniclastic in origin (Arculus et al., 2015b). This is the lithostratigraphic unit with the lowest average grain size and the highest number of magnetostratigraphic age constraints ($n = 86$). This allowed us to build a high-resolution age model for Unit I, which encompasses the last 24.3 Myr (Table S2). The absence of coarse-grained, gravity-flow volcaniclastic deposits indicates that Unit I has a predominant hemipelagic origin, with a minor contribution of far-traveling ash from nearby volcanic arcs of southwest Japan and, perhaps, the Izu-Bonin-Mariana arc that developed further east after the demise of the Kyushu-Palau Ridge.

The base of Unit I, now dated to 24.3 Ma, marks the end of the rifting phase of the Kyushu-Palau arc and its ultimate shutdown (Figure 5j). Since then, the area of the Amami-Sankaku basin adjacent to Site U1438 has been sourced with hemipelagic deposits at a low sedimentation rate ranging from 0.2 to 5.1 cm/kyr (0.8 cm/kyr on average; Table S2). The downhole variation of sedimentation rate in Unit I is, however, not progressive as expected but shows a sharp decrease from ∼2 to 0.5 cm/kyr over a short interval between approximately 80 and 90 mbsf (Table S2). This variation occurs immediately above the "initial compaction window" at 93–113 mbsf documented by Maffione and Morris (2017), which is the depth at which the sediments of Unit I develop a strong planar fabric (i.e., a sedimentary fabric) as a response to nonlinear compaction. This implies that the rapid decrease of sedimentation rates at 80–90 mbsf cannot be related to compaction (which seems to start further downhole at 93–113 mbsf), but is rather the effect of a downhole decrease in sediment supply occurring within this interval that can now be dated to 6.9–5.2 Ma.

A number of discrete ash layers were documented from Unit I (Arculus et al., 2015b). As demonstrated by Cambray et al. (1993), ash layers in deep-sea sediments may provide a reliable record of arc volcanism. Based on this assumption, we dated the 46 ash layers from Unit I (Table S4) with the aim to integrate the existing onshore record of southwest Japan volcanic activity with new offshore data. From the analysis of onshore volcanic products from southwest Japan, Kimura et al. (2003) identified four major volcanic stages: (a) An initial stage at 26–20 Ma; (b) an expansion stage at 20–12 Ma; (c) a tertiary volcanic arc stage at 12–4 Ma; and (d) a quaternary volcanic arc stage at 3–0 Ma.

The ash layers in Unit I range in thickness from 1 to 16 cm and are mainly concentrated at the top (0–70 mbsf) and bottom (125–161 mbsf) of Unit I (Table S4). Considering each ash layer as the product of a single volcanic eruption, we infer that neither the number of volcanic events nor the interval between two consecutive events are distributed homogeneously over the last 24.3 Myr (Table S4), but rather mark two distinct periods: An older period between 24.3 and 4.1 Ma characterized by fewer and less frequent volcanic eruptions, with 14 events occurring every 1.27 Myr, on average, and a recent period spanning the last 4.1 Myr characterized by more numerous and more frequent eruptions, with 32 events occurring every 0.13 Myr on average (Figure S5 in Supporting Information S1 and Table S4). We speculate that at approximately 4.1 Ma, either the activity of an existing volcanic center increased or a new volcanic edifice developed close to Site U1438 (e.g., in south Japan). The increase of volcanic activity in this region in the last 4.1 Myr may partly have contributed to the observed increase of sediment supply in the last 6.9 Myr highlighted by the sedimentation rates.

Finally, although the cores from Unit I has an azimuthal control that allowed to determine the *in situ* remanence directions (i.e., declination and inclination) for the past 24.3 Myr, these directions can only provide a rough approximation of the debated rotation of the PSP (e.g., Richter & Ali, 2015) due to the relatively high uncertainty of the FlexIT tool-corrected declinations. A different approach would be needed to use the paleomagnetic directions at Site U1438 and calculate the motion of the PSP over the past 50 Myr.

6. Conclusions

A high-resolution magnetostratigraphy based on 115 correlated reversals was produced for the ~1,600-m-thick suite of sedimentary and volcanic rocks recovered by IODP Expedition 351 at Site U1438 in the Amami-Sankaku basin, West Philippine Basin. The age model resulting from our magnetostratigraphy encompass the last 48.7 Myr and reveals that a ~1,460-m-thick hemipelagic and volcaniclastic sedimentary succession (Units I–IV) was deposited in a rear-arc position as a result of the emplacement, grow, and demise of the Kyushu-Palau volcanic arc above the nascent Izu-Bonin-Mariana subduction. Our age model and the calculated sedimentation rates at Site U1438 provide a precise temporal frame to the main tectono-magmatic events that occurred in the Philippine Sea Plate since subduction inception. Soon after subduction initiation at 52–50 Ma, and the emplacement of new oceanic crust (Unit 1) at 48.7 Ma, a mix of pelagic and volcaniclastic layers (Unit IV) was deposited between 48.7 and 43.3 Ma. This unit recorded the initial stage of prearc magmatic activity at 48.4–45.6 Ma, when boninites were being erupted in the forearc. Since 40.2 Ma, a fully developed Kyushu-Palau volcanic arc started shedding volcaniclastic deposits (Unit III) into the rear-arc Amami-Sankaku basin at an average rate of 29.7 cm/kyr and up to 72.5 cm/kyr. The growth of the Kyushu-Palau arc, at the specific location of IODP Site U1438, occurred through four main eruptive periods at 40.2–37.8, 37.1–35.2, 33.9–33.3, and 32.5–28.8 Ma. The volcanic activity of the arc decreased drastically at 28.8 Ma due to initial rifting of the arc, which continued until 24.3 Ma. During the rifting period the dying Kyushu-Palau arc continued to shed volcaniclastic sediments in the Amami-Sankaku basin (Unit II) but at a much lower sedimentation rate of 3.5 cm/kyr on average. Since 24.3 Ma, the Shikoku and Parece Vela back-arc basins started to open to the east of the (now relic) Kyushu-Palau arc and hemipelagic sedimentation continued until present at low sedimentation rates of less than 0.8 cm/kyr on average (Unit I). Finally the numerous ash layers present in Unit I combined with the high resolution of our magnetostratigraphy for this unit allowed a detailed characterization of the time and frequency of the volcanic activity of south Japan in the past 24 Myr.

Data Availability Statement

The demagnetization data and the calculated paleomagnetic directions used for the magnetostratigraphy of Site U1438 are available at figshare repository via https://doi.org/10.6084/m9.figshare.19794646.

References

Acton, G. D., Okada, M., Clement, B. M., Lund, S. P., & Williams, T. (2002). Paleomagnetic overprints in ocean sediment cores and their relationship to shear deformation caused by piston coring. *Journal of Geophysical Research*, *107*(B4), EPM3-1–EPM3-15. https://doi.org/10.1029/2001jb000518

Arculus, R., Ishizuka, O., Bogus, K. A., Gurnis, M., Hickey-Vargas, R., Aljahdali, M. H., et al. (2015a). A record of spontaneous subduction initiation in the Izu-Bonin-Mariana arc. *Nature Geoscience*, *8*(9), 728–733. https://doi.org/10.1038/ngeo2515

Arculus, R. J., Ishizuka, O., Bogus, K., Aljahdali, M. H., Bandini-Maeder, A. N., Barth, A. P., et al. (2015b). Expedition 351 methods. In R. J. Arculus, O. Ishizuka, K. Bogus, & the Expedition 351 Scientists (Eds.), *Proceedings of the International Ocean Discovery Program, expedition 351: Izu-Bonin-Mariana arc origins*. International Ocean Discovery Program. https://doi.org/10.14379/iodp.proc.351.102.2015

Arculus, R. J., Ishizuka, O., Bogus, K., Aljahdali, M. H., Bandini-Maeder, A. N., Barth, A. P., et al. (2015c). Site U1438. In R. J. Arculus, O. Ishizuka, K. Bogus, & the Expedition 351 Scientists (Eds.), *Proceedings of the International Ocean Discovery Program, expedition 351: Izu-Bonin-Mariana arc origins*. International Ocean Discovery Program.

Barth, A. P., Tani, K., Meffre, S., Wooden, J. L., Coble, M. A., Arculus, R. J., et al. (2017). Generation of silicic melts in the early Izu-Bonin arc recorded by detrital zircons in proximal arc volcaniclastic rocks from the Philippine Sea. *Geochemistry, Geophysics, Geosystems*, *18*(10), 3576–3591. https://doi.org/10.1002/2017GC006948

Brandl, P. A., Hamada, M., Arculus, R. J., Johnson, K., Marsaglia, K. M., Savov, I. P., et al. (2017). The arc arises: The links between volcanic output, arc evolution and melt composition. *Earth and Planetary Science Letters*, *461*, 73–84. https://doi.org/10.1016/j.epsl.2016.12.027

Cambray, H., Cadet, J. P., & Pouclet, A. (1993). Ash layers in deep-sea sediments as tracers of arc volcanic activity: Japan and central America as case studies. *Island Arc*, *2*(2), 72–86. https://doi.org/10.1111/j.1440-1738.1993.tb00075.x

Channell, J. E. T., & Guyodo, Y. (2004). The Matuyama Chronozone at ODP site 982 (Rockall Bank): Evidence for decimeter-scale magnetization lock-in depths. *Geophysical Monograph Series*, *145*(1), 205–219. https://doi.org/10.1029/145GM15

Channell, J. E. T., Harrison, R. J., Lascu, I., McCave, I. N., Hibbert, F. D., & Austin, W. E. N. (2016). Magnetic record of deglaciation using FORC-PCA, sortable-silt grain size, and magnetic excursion at 26 ka, from the Rockall Trough (NE Atlantic). *Geochemistry, Geophysics, Geosystems*, *17*(5), 1823–1841. https://doi.org/10.1002/2016GC006300

Channell, J. E. T., & Raymo, M. E. (2003). Paleomagnetic record at ODP site 980 (Feni Drift, Rockall) for the past 1.2 Myrs. *Geochemistry, Geophysics, Geosystems*, *4*(4), 1033. https://doi.org/10.1029/2002GC000440

Channell, J. E. T., Singer, B. S., & Jicha, B. R. (2020). Timing of quaternary geomagnetic reversals and excursions in volcanic and sedimentary archives. *Quaternary Science Reviews*, *228*, 106114. https://doi.org/10.1016/j.quascirev.2019.106114

Deschamps, A., Monié, P., Lallemand, S., Hsu, S.-K., & Yeh, K. Y. (2000). Evidence for early cretaceous oceanic crust trapped in the Philippine Sea plate. *Earth and Planetary Science Letters*, *179*(3–4), 503–516. https://doi.org/10.1016/S0012-821X(00)00136-9

Dunlop, D. J., & Özdemir, Ö. (1997). *Rock magnetism: Fundamentals and frontiers (No. 3)*. Cambridge university press.

Egli, R. (2003a). Analysis of the field dependence of remanent magnetization curves. *Journal of Geophysical Research*, *108*(B2), 2081. https://doi.org/10.1029/2002jb002023

Egli, R. (2003b). Environmental influences on the magnetic properties of lake sedimentsDoctoral dissertation. *ETH Zurich*. .

Harford, C. L., Pringle, M. S., Sparks, R. S. J., & Young, S. R. (2002). The volcanic evolution of Montserrat using $^{40}Ar/^{39}Ar$ geochronology. *Geological Society Memoir*, *21*(1), 93–113. https://doi.org/10.1144/gsl.mem.2002.021.01.05

Heslop, D., Dekkers, M. J., Kruiver, P. P., & van Oorschot, I. H. M. (2002). Analysis of isothermal remanent magnetization acquisition curves using the expectation-maximization algorithm. *Geophysical Journal International*, *148*(1), 58–64. https://doi.org/10.1046/j.0956-540x.2001.01558.x

Heslop, D., & Roberts, A. P. (2016). Analyzing paleomagnetic data: To anchor or not to anchor? *Journal of Geophysical Research: Solid Earth*, *121*(11), 7742–7753. https://doi.org/10.1002/2016jb013387

Hickey-Vargas, R. (2005). Basalt and tonalite from the Amami Plateau, northern West Philippine Basin: New early cretaceous ages and geochemical results, and their petrologic and tectonic implications. *Island Arc*, *14*(4), 653–665. https://doi.org/10.1111/j.1440-1738.2005.00474.x

Hickey-Vargas, R., Yogodzinski, G. M., Ishizuka, O., McCarthy, A., Bizimis, M., Kusano, Y., et al. (2018). Origin of depleted basalts during subduction initiation and early development of the Izu-Bonin-Mariana island arc: Evidence from IODP expedition 351 site U1438, Amami-Sankaku basin. *Geochimica et Cosmochimica Acta*, *229*, 85–111. https://doi.org/10.1016/j.gca.2018.03.007

Hilde, T. W., & Chao-Shing, L. (1984). Origin and evolution of the West Philippine Basin: A new interpretation. *Tectonophysics*, *102*(1–4), 85–104. https://doi.org/10.1016/0040-1951(84)90009-x

Ishizuka, O., Hickey-vargas, R., Arculus, R. J., Yogodzinski, G. M., Savov, I. P., Kusano, Y., et al. (2018). Age of Izu – Bonin – Mariana arc basement. *Earth and Planetary Science Letters*, *481*, 80–90. https://doi.org/10.1016/j.epsl.2017.10.023

Ishizuka, O., Tani, K., Reagan, M. K., Kanayama, K., Umino, S., Harigane, Y., et al. (2011). The timescales of subduction initiation and subsequent evolution of an oceanic island arc. *Earth and Planetary Science Letters*, *306*(3–4), 229–240. https://doi.org/10.1016/j.epsl.2011.04.006

Ishizuka, O., Taylor, R. N., Yuasa, M., & Ohara, Y. (2011). Making and breaking an island arc: A new perspective from the Oligocene Kyushu-Palau arc, Philippine Sea. *Geochemistry, Geophysics, Geosystems*, *12*(5), 1–40. https://doi.org/10.1029/2010GC003440

Johnson, K., Marsaglia, K. M., Brandl, P. A., Barth, A. P., Waldman, R., Ishizuka, O., et al. (2021). Intra-oceanic submarine arc evolution recorded in an ~1-km-thick rear-arc succession of distal volcaniclastic lobe deposits. *Geosphere*, *17*(4), 957–980. https://doi.org/10.1130/GES02321.1

Kasuga, S., & Ohara, Y. (1997). A new model of back-arc spreading in the Parece Vela Basin, northwest Pacific margin. *Island Arc*, *6*(3), 316–326. https://doi.org/10.1111/j.1440-1738.1997.tb00181.x

Kidane, T., Carlut, J., Courtillot, V., Gallet, Y., Quidelleur, X., Gillot, P. Y., & Haile, T. (1999). Paleomagnetic and geochronological identification of the Réunion subchron in Ethiopian Afar. *Journal of Geophysical Research*, *104*(B5), 10405–10419. https://doi.org/10.1029/1999jb900014

Kimura, J. I., Kunikiyo, T., Osaka, I., Nagao, T., Yamauchi, S., Kakubuchi, S., et al. (2003). Late Cenozoic volcanic activity in the Chugoku area, southwest Japan arc during back-arc basin opening and reinitiation of subduction. *Island Arc*, *12*(1), 22–45. https://doi.org/10.1046/j.1440-1738.2003.00377.x

Kirschvink, J. L. (1980). The least-squares line and plane and the analysis of palaeomagnetic data. *Geophysical Journal of the Royal Astronomical Society*, *62*(3), 699–718. https://doi.org/10.1111/j.1365-246X.1980.tb02601.x

Koymans, M. R., Langereis, C. G., Pastor-Galán, D., & van Hinsbergen, D. J. J. (2016). Paleomagnetism.org: An online multi-platform open source environment for paleomagnetic data analysis. *Computers & Geosciences*, *93*, 127–137. https://doi.org/10.1016/j.cageo.2016.05.007

Kruiver, P. P., Dekkers, M. J., & Heslop, D. (2001). Quantification of magnetic coercivity components by the analysis of acquisition curves of isothermal remanent magnetisation. *Earth and Planetary Science Letters*, *189*(3), 269–276. https://doi.org/10.1016/s0012-821x(01)00367-3

Maffione, M., & Herrero-Bervera, E. (2022). A relative paleointensity (RPI)-calibrated age model for the Corinth syn-rift sequence at IODP Hole M0079A (Gulf of Corinth, Greece). *Frontiers of Earth Science*, *10*, 813958. https://doi.org/10.3389/feart.2022.813958

Maffione, M., & Morris, A. (2017). The onset of fabric development in deep marine sediments. *Earth and Planetary Science Letters*, *474*, 32–39. https://doi.org/10.1016/j.epsl.2017.06.018

Mankinen, E. A., & Dalrymple, G. B. (1979). Revised geomagnetic polarity time scale for the interval 0-5 m.y. B.P. *Journal of Geophysical Research*, *84*(B2), 615–626. https://doi.org/10.1029/jb084ib02p00615

Maxbauer, D. P., Feinberg, J. M., & Fox, D. L. (2016). Max UnMix: A web application for unmixing magnetic coercivity distributions. *Computers & Geosciences*, *95*, 140–145. https://doi.org/10.1016/j.cageo.2016.07.009

McNeill, L. C., Shillington, D. J., Carter, G. D. O., Everest, J. D., Gawthorpe, R. L., Miller, C., et al. (2019). High-resolution record reveals climate-driven environmental and sedimentary changes in an active rift. *Scientific Reports*, *9*(1), 3116. https://doi.org/10.1038/s41598-019-40022-w

Ogg, J. G. (2020). Chapter 5: Geomagnetic polarity time scale. In F. M. Gradstein, J. G. Ogg, M. D. Schmitz, & G. M. Ogg (Eds.), edited by *Geological time scale 2020*, (pp. 159–192). Elsevier.

Okino, K., Kasuga, S., & Ohara, Y. (1998). A new scenario of the Parece Vela basin Genesis. *Marine Geophysical Research*, *20*(1), 21–40. https://doi.org/10.1023/A:1004377422118

Okino, K., Ohara, Y., Kasuga, S., & Kato, Y. (1999). The Philippine Sea: New survey results reveal the structure and the history of the marginal basins. *Geophysical Research Letters*, *26*(15), 2287–2290. https://doi.org/10.1029/1999GL900537

Okino, K., Shimakawa, Y., & Nagaoka, S. (1994). Evolution of the Shikoku Basin. *Journal of Geomagnetism and Geoelectricity*, *46*(6), 463–479. https://doi.org/10.5636/jgg.46.463

Peters, C., & Dekkers, M. J. (2003). Selected room temperature magnetic parameters as a function of mineralogy, concentration and grain size. *Physics and Chemistry of the Earth*, *28*(16–19), 659–667. https://doi.org/10.1016/s1474-7065(03)00120-7

Petrovský, E., & Kapička, A. (2006). On determination of the Curie point from thermomagnetic curves. *Journal of Geophysical Research*, *111*(12), 1–10. https://doi.org/10.1029/2006JB004507

Prueher, L. M., & Rea, D. K. (2001). Tephrochronology of the Kamchatka-Kurile and Aleutian arcs: Evidence for volcanic episodity. *Journal of Volcanology and Geothermal Research*, *106*(1–2), 67–84. https://doi.org/10.1016/S0377-0273(00)00266-3

Reagan, M. K., Heaton, D. E., Schmitz, M. D., Pearce, J. A., Shervais, J. W., & Koppers, A. A. P. (2019). Forearc ages reveal extensive short-lived and rapid seafloor spreading following subduction initiation. *Earth and Planetary Science Letters*, *506*, 520–529. https://doi.org/10.1016/j.epsl.2018.11.020

Reagan, M. K., Ishizuka, O., Stern, R. J., Kelley, K. A., Ohara, Y., Blichert-Toft, J., et al. (2010). Fore-arc basalts and subduction initiation in the Izu-Bonin-Mariana system. *Geochemistry, Geophysics, Geosystems*, *11*(3), 1–17. https://doi.org/10.1029/2009GC002871

Reagan, M. K., Pearce, J. A., Petronotis, K., Almeev, R., Avery, A. A., Carvallo, C., et al. (2015). Expedition 352 summary. In M. K. Reagan, J. A. Pearce, K. Petronotis, & the Expedition 352 Scientists (Eds.), *Izu-bonin-mariana fore arc. Proceedings of the International Ocean Discovery Program, 352*. International Ocean Discovery Program. https://doi.org/10.14379/iodp.proc.352.101.2015

Richter, C., & Ali, J. R. (2015). Philippine Sea Plate motion history: Eocene-Recent record from ODP Site 1201, central West Philippine basin. *Earth and Planetary Science Letters*, *410*, 165–173. https://doi.org/10.1016/j.epsl.2014.11.032

Rivera, T. A., Schmitz, M. D., Crowley, J. L., & Storey, M. (2014). Rapid magma evolution constrained by zircon petrochronology and $^{40}Ar/^{39}Ar$ sanidine ages for the Huckleberry Ridge Tuff, Yellowstone, USA. *Geology*, *42*(8), 643–646. https://doi.org/10.1130/G35808.1

Savov, I. P., Hickey-Vargas, R., D'Antonio, M., Ryan, J. G., & Spadea, P. (2006). Petrology and geochemistry of West Philippine Basin basalts and early Palau-Kyushu arc volcanic clasts from ODP Leg 195, site 1201D: Implications for the early history of the Izu-Bonin-Mariana arc. *Journal of Petrology*, *47*(2), 277–299. https://doi.org/10.1093/petrology/egi075

Singer, B. S. (2014). A quaternary geomagnetic instability time scale. *Quaternary Geochronology*, *21*(1), 29–52. https://doi.org/10.1016/j.quageo.2013.10.003

Stern, R. J., & Bloomer, S. H. (1992). Subduction zone infancy: Examples from the Eocene Izu-Bonin-Mariana and Jurassic California arcs. *The Geological Society of America Bulletin*, *104*(12), 1621–1636. https://doi.org/10.1130/0016-7606(1992)104<1621:szieft>2.3.co;2

Van Hinte, J. E. (1978). Geohistory analysis – Application of micropaleontology to exploration geology. *The American Association of Petroleum Geologists Bulletin*, *62*, 201–222. https://doi.org/10.1306/C1EA4815-16C9-11D7-8645000102C1865D

Waldman, R. J., Marsaglia, K. M., Hickey-Vargas, R., Ishizuka, O., Johnson, K. E., McCarthy, A., et al. (2021). Sedimentary and volcanic record of the nascent Izu-Bonin-Mariana arc from IODP site U1438. *Bulletin of the Geological Society of America*, *133*(7–8), 1421–1440. https://doi.org/10.1130/B35612.1

Wang, L., Pan, Y., Li, J., & Qin, H. (2008). Magnetic properties related to thermal treatment of pyrite. *Science in China - Series D: Earth Sciences*, *51*(8), 1144–1153. https://doi.org/10.1007/s11430-008-0083-7

Watt, S. F. L., Talling, P. J., Vardy, M. E., Heller, V., Hühnerbach, V., Urlaub, M., et al. (2012). Combinations of volcanic-flank and seafloor-sediment failure offshore Montserrat, and their implications for tsunami generation. *Earth and Planetary Science Letters*, *319–320*, 228–240. https://doi.org/10.1016/j.epsl.2011.11.032

Wu, J., Suppe, J., Lu, R., & Kanda, R. (2016). Philippine Sea and East Asian plate tectonics since 52 Ma constrained by new subducted slab reconstruction methods. *Journal of Geophysical Research: Solid Earth*, *121*(6), 4670–4741. https://doi.org/10.1002/2016JB012923

Yogodzinski, G. M., Bizimis, M., Hickey-Vargas, R., McCarthy, A., Hocking, B. D., Savov, I. P., et al. (2018). Implications of Eocene-age Philippine Sea and forearc basalts for initiation and early history of the Izu-Bonin-Mariana arc. *Geochimica et Cosmochimica Acta*, *228*, 136–156. https://doi.org/10.1016/j.gca.2018.02.047